TIMING CHARACTERISTICS OF INTERMEDIATE POLAR TYPE CATACLYSMIC VARIABLES AND DETAILED DATA ANALYSIS ON YY DRACONIS

118978

A THESIS SUBMITTED TO
THE GRADUATE SCHOOL OF NATURAL AND APPLIED SCIENCES
OF
THE MIDDLE EAST TECHNICAL UNIVERSITY

BY

EFE YAZGAN

118978

T.C. YÜKSEKÖĞRETİM KURULU
DOKÜMANTASYON MERKEZİ

IN PARTIAL FULFILLMENT OF THE REQUIREMENTS FOR THE DEGREE OF

MASTER OF SCIENCE

IN

THE DEPARTMENT OF PHYSICS

JANUARY 2002

Approval of the Graduate School of Natural and Applied Sciences.

Prof. Dr. Tayfur Öztürk
Director

I certify that this thesis satisfies all the requirements as a thesis for the degree of Master of Science.

Prof. Dr. Sinan Bilikmen
Head of Department

This is to certify that we have read this thesis and that in our opinion it is fully adequate, in scope and quality, as a thesis for the degree of Master of Science.

Assist. Prof. Dr. Şölen Balman
Supervisor

Examining Committee Members

Assist.Prof.Dr.Şölen Balman

Prof. Dr. Nilgün Kızıloğlu

Prof. Dr. Ümit Kızıloğlu

Prof. Dr. Altan Baykal

Prof. Dr. Oktay Hüseyin

ABSTRACT

TIMING CHARACTERISTICS OF INTERMEDIATE POLAR TYPE CATACLYSMIC VARIABLES AND DETAILED DATA ANALYSIS ON YY DRACONIS

YAZGAN, Efe

M.S., Department of Physics

Supervisor: Assist. Prof. Dr. Şölen Balman

January 2002, 77 pages.

In this thesis, an up-to-date review of intermediate type cataclysmic variables are made emphasizing timing characteristics. Fundamental timing analysis methods are introduced. Timing analysis on the intermediate polar AE Aquarii is performed using three sets of *ROSAT* archival data. We have done timing and spectral analysis on the intermediate polar YY Draconis using *ASCA* and *ROSAT* archival data sets. We have investigated the energetics of the pulse profiles. It is found that X-ray pulse profiles of YY Dra decreases with increasing energy. It is also found that the X-ray spectrum of YY Draconis can be represented by single or multitemperature bremsstrahlung and/or VMEKAL models. Lastly, the implication of our analysis is discussed in the light of current theory and observations.

Keywords: Cataclysmic Variables, Intermediate Polars, Timing Methods, Pulse Profiles, Spectral Analysis, AE Aquarii, YY Draconis

ÖZ

ORTA ŞİDDETLİ MANYETİK ALANLI KATAKLİZMİK DEĞİŞKENLERİN YENİDEN GÖZDEN GEÇİRİLMESİ VE YY DRACONIS ÜSTÜNE AYRINTILI VERİ ARAŞTIRMASI

YAZGAN, Efe

Yüksek Lisans, Fizik Bölümü

Tez Yöneticisi: Assist. Prof. Dr. Şölen Balman

Ocak 2002, 77 sayfa.

Bu tezde, Orta Dereceli Manyetik Alanlı Kataklizmik Değişkenlerin (ODMKD) genel X-ışını verileri zamansal özelliklere önem verilerek güncelleştirilmiş ve temel zamansal araştırma yöntemleri tartışılmıştır. ODMKD AE Aquarii'nin zamansal analizi ROSAT ile alınmış üç arşiv veri kümesi kullanılarak yapılmıştır. Bir diğer ODMKD olan YY Draconis için ayrıntılı zaman ve tayf analizi yapılmıştır. Atım özyapılarının enerji bağımlılıkları incelenmiştir ve atım genliğinin enerji arttıkça arttığı bulunmuştur. YY Draconis'in X-ışını tayfı tek ve çok sıcaklıklı bremsstrahlung ve VMEKAL modelleriyle uyumlu olduğ gösterilmiştir. Bulunan sonuçların önemi ve getirdikleri günümüzün gözlemsel ve teorik çerçevelerinde tartışılmış ve açıklanmaya çalışılmıştır.

Anahtar Kelimeler: Kataklizmik Değişkenler, Orta Dereceli Manyetik Alanlı Kataklizmik Değişkenler, Zamanlama Yöntemleri, Atım Özyapıları, Tayf Analizi, AE Aquarii, YY Draconis

ACKNOWLEDGMENTS

I express my deepest gratitude to Assist. Prof. Dr. Şölen Balman Balman for her guidance throughout the research.

I would like to thank Prof. Dr. Ümit Kızıloğlu and Prof. Dr. Altan Baykal for their fruitful discussions and helpful suggestions.

I thank my friends and colleagues in METU Astrophysics Group and TÜBİTAK High Energy Astrophysics Unit for their support, S. Çağdaş İnam and Özgür Taşkın for their technical support and for their friendship and my parents for their moral and economical support.

I especially thank my wife, Yasemin, for her love and encouragement.

I acknowledge a scholarship provided by Turkish Scientific Research Council (TÜBİTAK).

TABLE OF CONTENTS

ABSTRACT iii

ÖZ v

ACKNOWLEDGMENTS vii

TABLE OF CONTENTS viii

LIST OF TABLES x

LIST OF FIGURES xi

CHAPTER

1 Introduction 1

2 Timing Characteristics of Intermediate Polars 10

2.1 Spin and Orbital Periods 10

2.2 X-ray Flux 12

2.3 Spin Period Changes 13

2.4 Orbital Sidebands 15

2.5 X-Ray Pulse Profiles and The Geometry of the Accretion Column 16

3 Power Spectral Methods for Astronomical Timing Analysis 26

3.1 Power Spectrum 26

3.1.1 Basic Definitions 26

3.1.2 Statistics of the Power Spectrum 27

3.2 Lomb-Scargle Periodogram Analysis 28

3.2.1 Definition 28

3.2.2 Statistics and Computation 29

3.3 Fast Fourier Transform (FFT) 31
3.4 Cross-Correlation 32

4 ROSAT Timing Analysis of AE Aquarii 35
4.1 AE Aquarii 35
4.2 Data Analysis 36
4.2.1 Spin-Period of the White Dwarf in AE Aquarii . 36
4.2.2 Pulse-Profiles of AE Aquarii 37

5 Spectral and Temporal Analysis of the Intermediate Polar YY Dra in the Energy Range 0.1-10 keV 43
5.1 Introduction 43
5.2 Observations and Data 45
5.3 Temporal Analysis 46
5.4 X-Ray Spectra 48
5.4.1 Spectral Models 48
5.4.2 Spectra of YY Dra 50
5.5 Discussion 52
5.5.1 The X-ray Pulse Profiles 52
5.5.2 The Spectrum (0.1-10 keV) 55

6 DISCUSSION AND CONCLUSIONS 68

REFERENCES 71

LIST OF TABLES

TABLE

2.1 Timing data for Intermediate Polars 19
2.2 Timing data for Intermediate Polars 20
2.3 Timing data for Intermediate Polars 21

5.1 Single-temperature bremsstrahlung and VMEKAL model parameters 59
5.2 Two-temperature bremsstrahlung and VMEKAL model parameters 59
5.3 Simultaneous fitting of ASCA and ROSAT Data 60

LIST OF FIGURES

FIGURE

1.1 The Roche equipotentials of a test particle under the influence of two massive gravitating objects. 5

1.2 Birth of an accretion disk. 6

1.3 3-D Geometry of a non-magnetic cataclysmic variable. 7

1.4 Side-view of an intermediate polar type cataclysmic variable. . . 8

1.5 Geometry of a polar type cataclysmic variable. 8

1.6 Accretion on to the surface of a WD via a boundary layer 9

2.1 Galactic Distribution of Intermediate Polars 22

2.2 Spin Period Distribution of Intermediate Polars 22

2.3 Orbital Period Distribution of Intermediate Polars 23

2.4 Spin Period vs. Orbital Period 23

2.5 $P - \dot{P}$ Diagram for Intermediate Polars 24

2.6 X-Ray Flux vs. Orbital Period 24

2.7 X-Ray Flux vs. Spin Period 25

3.1 Detection level vs. number of trials 34

4.1 Power Spectrum of AE Aqr from the ROSAT observation in 10-16 November 1992 39

4.2 Power Spectrum of AE Aqr from the ROSAT observation in 20-21 October 1993 40

4.3 Pulse Shapes of ROSAT data of AE AQR taken between 10-16 November 1992 41

4.4 Pulse Shapes of ROSAT PSPC data of AE AQR taken between 20-21 October 1993 42

5.1 X-ray light curve of YY Dra in 100 sec bins 61
5.2 The Power Spectrum of YY Dra 62
5.3 The energy dependent folded pulse profiles of YY Dra obtained from the GIS3 data folded on the 264.6 s period 63
5.4 The energy dependent folded pulse profiles of YY Dra obtained from the GIS3 data folded on the 529.2 s period 64
5.5 The X-ray data of YY Dra fit with a single-temperature VMEKAL model 65
5.6 The energy dependent folded pulse profiles of YY Dra obtained from ROSAT HRI data 66
5.7 The combined spectrum of ROSAT (HRI) and ASCA (SIS) data . 67

CHAPTER 1

Introduction

A cataclysmic variable (CV) is a close interacting binary system in which a white dwarf (WD) accretes material from its late-type low mass main sequence companion. CVs can be studied in two main classes: non-magnetic CVs that are characterized by their eruptive behaviour and magnetic CVs (MCVs). Two populated sub-classes of MCVs are distinguished according to the degree of synchronization of orbit of the binary. If a system is highly synchronized, then it is called a Polar type MCV or an AM Her star; otherwise it is called an Intermediate Polar (IP). A sub-type of IPs is the DQ Her stars. Synchronization of the orbit is caused by tidal forces acting on the companion star and by the interaction of the magnetic fields of the WD and the companion star. Tidal forces, in general wash out the eccentric orbits in CVs. The timescale of tidal forces in CVs is much shorter than the CV lifetime. In the evolutionary sequence, the radius of the companion star increases considerably and then the outer layers of the envelope of the companion star is accreted by the WD. This process is called Roche lobe overflow. Roche lobe is defined through the analysis of the restricted three-body problem. In this

analysis, the motion of a light test particle under the influence of two massive bodies bound via gravitational force in a circular orbit, is investigated. The test particle is much lighter than the other two bodies that the two heavy bodies orbit around each other in such a plane that would not occur in the interaction of three bodies with comparable masses. The Roche analysis is suitable for CVs (as for other binary systems), because the three fundamental assumptions are more or less met in these systems. Namely, the orbit of CVs are circular in general due to the tidal effects mentioned above; the third body, which is the envelope of the companion star, is much less than the mass of the other bodies in the system (stars), and the stars can be considered as point masses when considering the dynamics of the accretion. If we consider a binary system with masses of the components M_1 and M_2, and ratio of the masses denoted by $q=M_2/M_1$, the separation of the circular orbit a, and the orbital frequency are given by

$$\Omega^2 = \frac{G(M_1 + M_2)}{a^3} \tag{1.1}$$

$$a = 3.5 \times 10^{10} cm M_1^{1/3} (1+q)^{1/3} P_{hr}^{2/3} \tag{1.2}$$

where P_{hr} is the period of the orbit in hours. Note that, the binary separation a is less than the radius of the sun which is $R_\odot = 7 \times 10^{10}$ cm. In the corotating frame (with the binary), the equation of motion of a test paticle is

$$\frac{d\mathbf{v}}{dt} = -\nabla\phi_R + 2\mathbf{v} \times \mathbf{\Omega} \tag{1.3}$$

The second term on the right hand side of the above equation represents the coriolis force and

$$\phi_R = -\frac{GM_1}{|\mathbf{r}-\mathbf{r_1}|} - \frac{GM_2}{|\mathbf{r}-\mathbf{r_2}|} - \frac{1}{2}(\Omega \times \mathbf{r})^2 \tag{1.4}$$

is called the Roche potential, which represents the effects of the gravitational forces of individual stars on the test particle and also the effect of the centrifugal force. The equipotential surfaces of the Roche potential on the orbital plane is displayed in Figure 1.1. There are five equilibrium points (Lagrange points) of which L_1, L_2 and L_3 are unstable and L_4 and L_5 are stable points. In Figure 1.1, the *Roche Lobes* of the two stars in the binary system are represented with boldface curves connected at the *inner Lagrangian point* L_1. In a CV, the primary star is always a WD, so the primary star always lies in its Roche Lobe. However, the secondary star expands and exceeds its Roche Lobe, so that the matter outside the Roche Lobe of the secondary is captured by the primary star. The shape of the star is no longer spherical after filling its Roche Lobe, it attains the shape of its Roche Lobe. CVs are called *semi – detached* binaries due to the fact that only one of the components of the binary fills its Roche Lobe.

The initial gas stream passes the L_1 point towards the WD and forms an ellipse-like ring, then becomes a circular ring due to the conservation of angular momentum. Meanwhile, the ring of gas spreads with velocity of sound and an accretion disk is formed. The initial stages of the formation of an accretion disk is described in Figure 1.2. If the WD in the binary system has a weak magnetic field, then the accretion disk extends down to the surface of the WD. In the

case of magnetic WDs, however, the disk is truncated and the gas is forced to follow the magnetic field lines of the WD at around the so called Alfven radius. Alfven radius is defined to be the radius beyond which the magnetic pressure of the magnetosphere of the WD exceeds the gas pressure in the accreting gas. Assuming the magnetic pressure and gas pressure equal to each other, the Alfven radius is found as

$$r_A = 5.1 \times 10^8 \dot{M}_{16}^{-2/7} M_1^{-1/7} \mu_{30}^{4/7} cm \tag{1.5}$$

where $\dot{M}_{16}$ is the accretion rate in 10^{16} gr/s, M_1 is the mass of the WD in solar mass units and μ_{30} is the magnetic moment of the WD in units of 10^{30} G cm^3. In the case of IPs, a disk remains outside the Alfven radius, since the magnetic field strength of the WD in these systems are in a medium range. However, the final impact of the accreted gas happens on the magnetic poles of the WD. Polars have no accretion disk due to the large value of the Alfven radius which exceeds the L1 point of the binary. Different accretion geometries occuring in CVs described above are displayed in Figure 1.3, 1.4 and 1.5 .

The velocity of the plasma falling onto the WD surface is calculated to be in the range 3000-10000 km/s which is greater than the sonic speed ≈100 km/s in the plasma. Therefore, the infalling plasma releases its energy in a shock as it is coming to a stop within a boundary layer at the surface of the WD. The resulting shock has a temperature of T≈10^8 K and emits hard X-rays, ultraviolet (UV) and optical light. For magnetic CVs, the final impact of the plasma will be at the magnetic poles of the WD, which are believed to be inclined to the spin axis

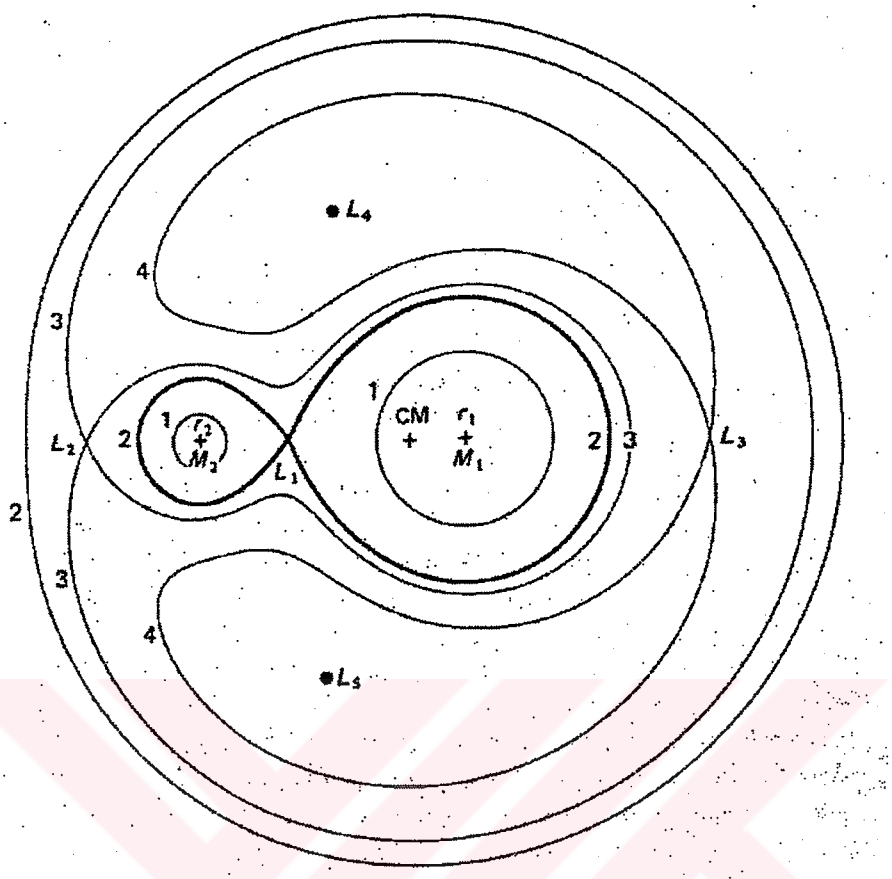


Figure 1.1: The Roche equipotentials of a test particle under the influence of two massive gravitating objects.

of the WD. This misalignment of the spin and magnetic axis causes a periodic modulation of the X-ray, UV and optical light detected at Earth, at the spin period, one of its harmonics (due to double pole accretion) or sidebands (due to the reprocessed light from structures fixed in the reference frame of the binary or material overflowing the disk). Figure 1.6 displays the final stage of the accretion onto the WD.

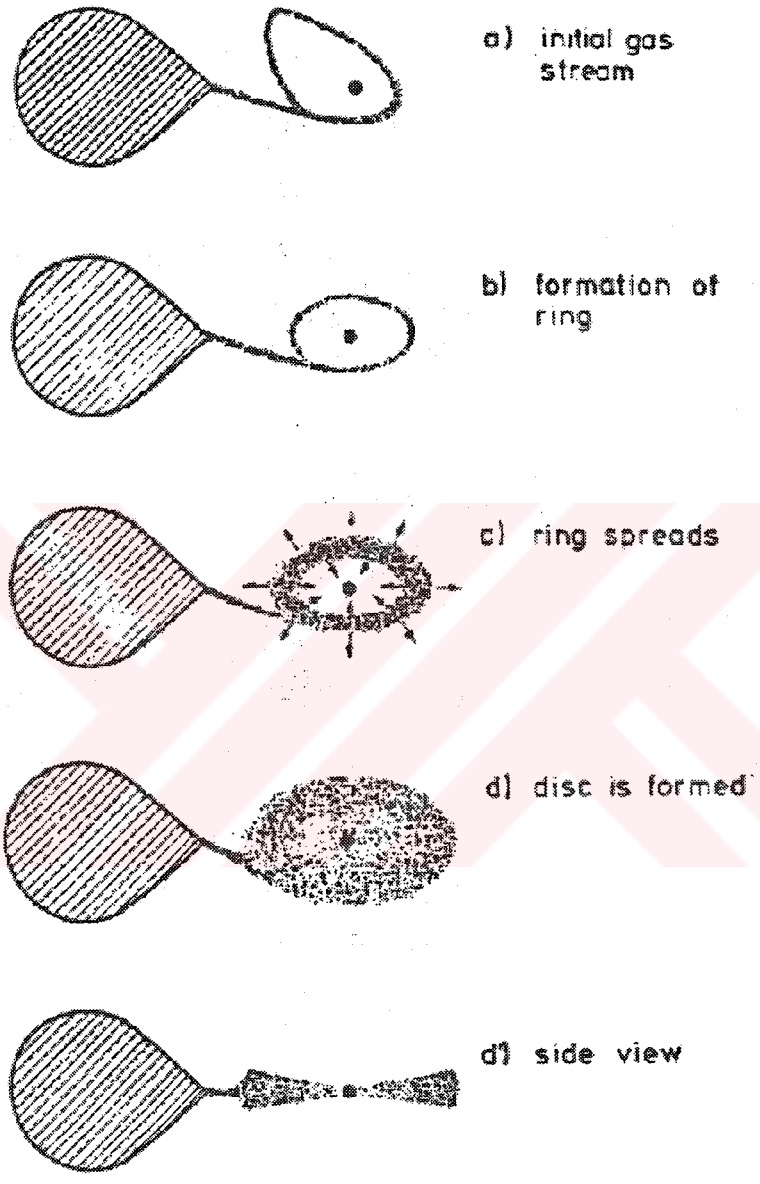


Figure 1.2: Birth of an accretion disk.

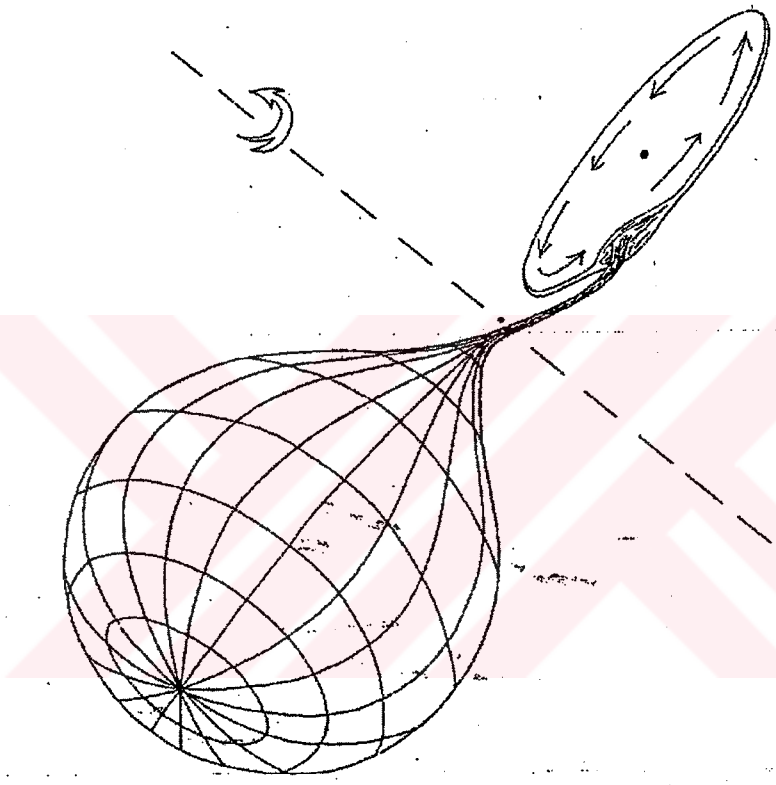


Figure 1.3: 3-D Geometry of a non-magnetic cataclysmic variable.

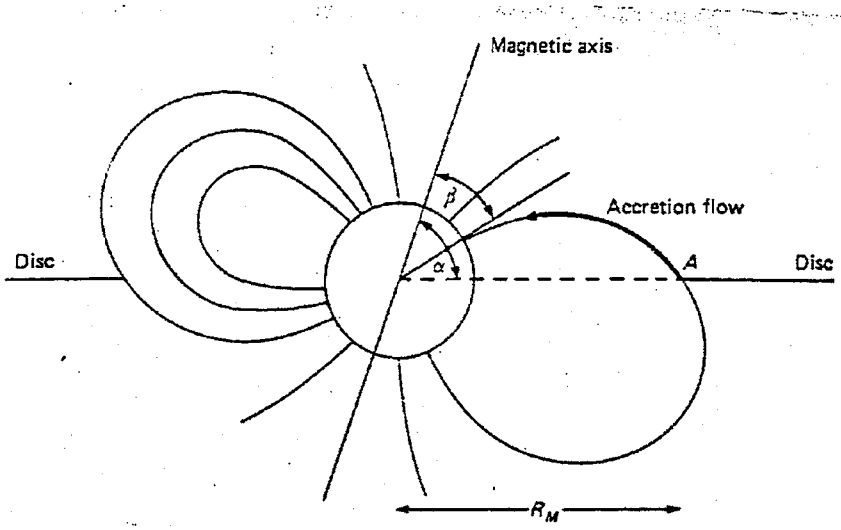


Figure 1.4: Side-view of an intermediate polar type cataclysmic variable.

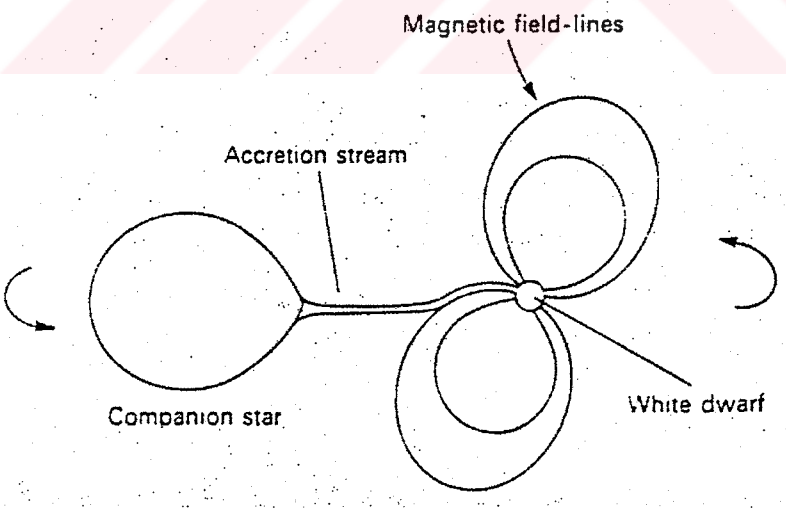


Figure 1.5: Geometry of a polar type cataclysmic variable.

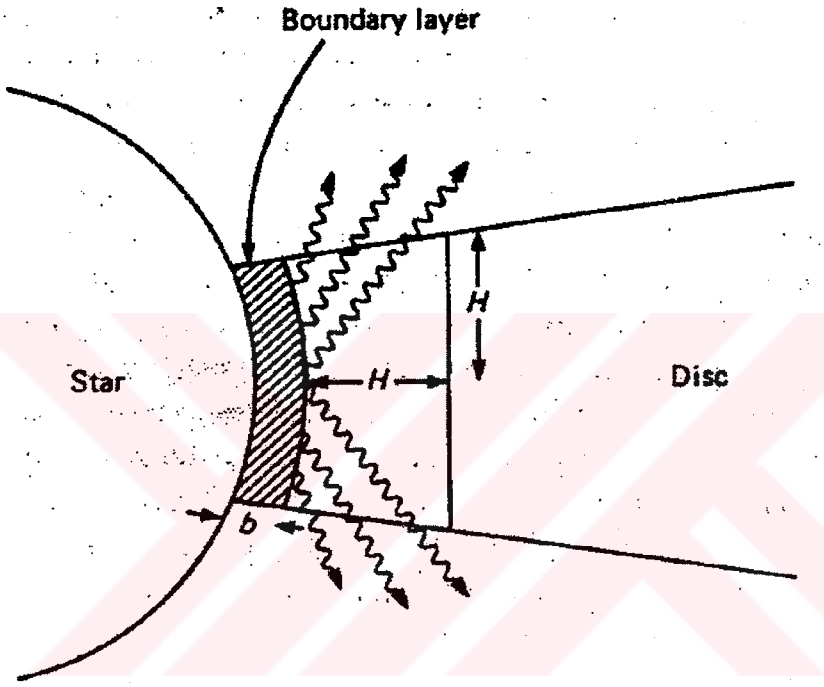


Figure 1.6: Accretion on to the surface of a WD via a boundary layer. H represents the typical scale height of the accretion column and b is the typical boundary layer thickness.

CHAPTER 2

Timing Characteristics of Intermediate Polars

The defining characteristics of IPs are the existence of stable periodicities in the optical and X-ray light curves, which can be attributed to spin and orbital periods. IPs have strong X-ray emission. X-ray and optical light curves of IPs display disk characteristics (as expected), like the existence of orbital side-band periods, existence of spin-up systems as well as spin down systems. We present a review of these emprical characteristics of IPs in this chapter,

2.1 Spin and Orbital Periods

We have gathered the fundamental timing data for IPs from the literature (published up to November 2001). In Table 1, period (P) in seconds, period derivative ($\dot{P}$) in 10^{-11}s/s and orbital period (P_{orb}) in hours are shown in second, third and forth columns respectively. In the second column, also, the presence of a first harmonic, sidebands and quasiperiodic oscillations are indicated by (1H), (SB) and (QPO), respectively. Figure 2.1 displays the Galactic distribution of the sources presented in Table 2.1. The figure shows a more or less homogeneous

sample of systems distributed in the Galaxy extending from l$\sim 0^o$ to 300^o and b$\sim$-55^o to 55^o. In general, IPs have spin periods less than their orbital periods, i.e. $P_{spin} < P_{orb}$. The orbital periods are in the range $\sim$1.4 hours to $\sim$47.9 hours. The spin periods of IPs range from $\sim$33 seconds to $\sim$7200 seconds. 79% of the spin periods lie below 2000 seconds. Figure 2.2 shows the spin period distribution of IPs. We see that the distribution peaks at $\sim$750 seconds. This peak is observationally significant since there seems to be no selection effects in period measurements of CVs, however physical significance of this peak is unclear. One hypothesis is that, the peak corresponds to the so called "equilibrium period" (see Ghosh & Lamb 1979a, 1979b, 1991 for the description of the equilibrium period). This hypothesis can be tested by long term $\dot{P}$ and $\ddot{P}$ measurements which should give the same equilibrium period. A prediction of this hypothesis is that, if the peak corresponds to the equilibrium period, then the systems having such periods must be older than the other IPs.

Figure 2.3 displays the orbital period distribution of IPs. Orbital periods cluster around 5 hrs with little dispersion. One exception is the system, GK Per which has a different type of secondary star. The clustering is expected because IPs have similar system parameters and binaries with similar parameters have similar orbital periods.

Spin periods are plotted against orbital periods in Figure 2.4, which shows that there is no simple mathematical relation between spin and orbital periods, contrary to the proposals Barrett et al. (1988), Warner and Wickramasinghe

(1991), Wickramasinghe et al. (1991) and King and Lasota (1991). The expectation of these authors was $P_{spin} = 0.1 P_{orbital}$ shown with a dotted line in Figure 2.4. The reason for the non-existence of such a relation might be due to the fact that similar systems show similar orbital periods, however depending on the $\dot{M}$ history, spin periods can take a more dispersed range of values than orbital periods. However, if we compare the peaks in the spin and orbital period distributions, we find $P_{spin} \sim 0.1 P_{orbital}$. If our hypothesis about the peak period in the spin distribution is correct, then the above relation shows that there exists a simple relation connecting the equilibrium period and the orbital period of an IP system. This would be a consequence of the fact that IPs are disk hosting systems and have similar orbital characteristics.

2.2 X-ray Flux

In Figure 2.6 quiescent X-ray flux (in 2-10 keV band) vs. orbital period is displayed. The data are taken from Patterson (1994). From the graph we see that maximum X-ray flux detected is $\sim 8 \times 10^{-11}$ erg cm^{-2} s^{-1}. All of the observed fluxes lie below the line $F_x = -[0.7 P_{orb} + 16.7] \times 10^{-11}$ erg cm^{-2} s^{-1}. GK Per is excluded which has a very long orbital period (47 hr) and stands in a very different place from other IPs in this diagram. A correlation or anti-correlation of the flux with orbital period is not expected, since most of the X-ray flux originate from the accretion column which has properties not depending on the accretion disk and the orbital period in the first approximation. As pointed out by Patterson (1994) IPs have lower hard X-ray luminosities than expected

by radial accretion. The explanation of this underluminosity might be that only $\sim 20\%$ of the disk material accretes radially and develope a shock. The remaining material accretes without developing a shock tunneling into the WD (Kuijpers and Pringle 1982; Thompson et al. 1986; Frank et al. 1988; Patterson 1994). If the amount of material not developing a shock is directly proportional to the angular momentum of the accretion disk, then we expect that IPs with low orbital periods (so the system posseses an accretion disk with high angular momentum) have low X-ray luminosities. But this is contrary to the observational results displayed in Figure 2.6. Thus, we conclude that the anticorrelation between the flux and the orbital period is only arising from the insufficient number of data.

In Figure 2.7 X-ray flux vs. spin period is displayed. This figure shows no obvious correlation. This is something expected, since we have a very complicated interaction between the magnetic WD and the accretion disk. Accretion process can have different phases depending on the spin period and/or the magnetic field structure of the WD.

2.3 Spin Period Changes

Because a WD has a small radius compared to the accretion disk, it has small enough moment of inertia to have period changes due to the torques applied on the WD by the disk. The period change of the WD is determined by the interaction of the WD magnetic field with the accreting plasma and the interaction of the WD with the matter torques applied by the disk. Away from the Alfven radius, the material in the disk circulates with Keplerian velocity. If the WD

rotates slower than the material near the magnetospheric radius, then the accreting material transfers its energy to the WD due to the angular momentum gradient in the direction from disk to the WD and consequently WD starts to rotate faster. However, above some rotation velocity of the WD, the angular momentum gradient is from the WD to the disk, so that the accreting material slows down the WD. The whole process is parametrized phenomenologically by a fastness parameter first introduced by Ghosh and Lamb (1987a,b):

$$\omega_s = \frac{\Omega_{WD}}{\Omega(R_{mag})} \tag{2.1}$$

Lamb (1988) found a critical value for $\omega_{crit} = 0.35 - 0.85$ for which if ω_s is smaller than the critical value, the star is called a slow rotator and spinning up. If ω_s is bigger, then the star spins down. Once the star's rotation is near ω_{crit}, the star is said to be in spin equilibrium and wanders around the equilibrium period in shorter timescales. The change of period is found as

$$\dot{P} = -1.7 \times 10^{-11} \mu_{32}^{4/7} M_{\odot}^{1.0} P_{1000}^{2} \dot{M}_{17}^{6/7} n(\omega_s) \tag{2.2}$$

where $n(\omega_s) \approx 1.4 \times [1 - (\omega_s/\omega_{crit})]/(1 - \omega_s)$ is the torque function (Ghosh & Lamb 1979 a,b), μ_{32} is the magnetic moment of the WD in scaled to 10^{32} erg/G, $M_{\odot}$ is the mass of the WD in Solar mass units, P_{1000} is the period of the WD scaled to 1000 seconds and $\dot{M}_{17}$ is the accretion rate scaled to 10^{17} g/s. The second derivative of the period may exist due to a changing accretion rate, so that $\ddot{P}$ can be related to $\ddot{M}$ dimensionally as

$$\ddot{P} \propto \ddot{M}(M_{WD}R_A)^{1/2} \tag{2.3}$$

where $\ddot{M}$ represents the time derivative of accretion rate, M_{WD} mass of the WD and R_A the Alfven radius.

We present in Figure 2.5, the $P - \dot{P}$ diagram for IPs, in which there are only a few number of data points. This is because, $\dot{P}$ measurements are hard to achieve due to the uncertainties in period values which must be compansated by long and continuous observations. This is especially hard in the X-ray band, since the observation times are restricted. However, continous monitoring of the optical pulses is possible and that would yield valuble information on the accretion disk-magnetosphere interactions and evolution of magnetic CV systems. We want to note that all of the values presented in the $P - \dot{P}$ diagram is determined in the optical band (with about 10 years of almost continuous observations, see Patterson 1994). We see that there are both spin-up and spin-down systems which shows that IPs are disk-accreting systems. The $\dot{P}$ values are consistent with the values given by equation 2.2 above.

2.4 Orbital Sidebands

Periodic modulations at orbital sidebands of the spin frequency are observed in 8 of the IPs listed in Table 2.1. These oscillations are detected in X-ray or optical bands. If we designate ω as the spin frequency and Ω as the orbital frequency, then observations show that there can exist variations in the X-ray light curve with frequencies $\omega - \Omega$, $\omega + \Omega$ and $\omega - 2\Omega$. One of the reasons for these frequencies is believed to be the overflow of some significant amount of the accreting material

over the disk, connecting directly to the field lines as a stream which flips between the poles of the WD on the beat period (Hellier 1991). Another reason might be the spiral shocks which can interact with the matter at the magnetosphere coupling in orbital phase Murray et al. (1999a). The disk-overflow model can explain the optical sidebands also. However, the reason of light curve variations at optical sidebands might be reprocessing of spin-pulsed X-rays by the secondary or the hot spot where the material leaving the secondary hits the accretion disk (Hellier, Cropper and Mason 1991; Wickramasinghe and Ferrario 1999).

2.5 X-Ray Pulse Profiles and The Geometry of the Accretion Column

X-ray pulse profiles give valuable information on how the plasma is accreted on the WD surface. Pulse profiles are produced by the rotating and radiating accretion column. Observations showed that the light curves of IPs are quasi-sinusoidal with dips superimposed (Norton et al. 1990, 1992a,b and Norton 1993). Most of the IP pulse profiles show a decrease in the modulation amplitude as energy is increased (Norton and Watson 1989; Shafter, Szkody and Thorstensen 1986; Mason et al. 1992) with one exception; YY Dra (this work, Chapter 5) which shows an increase in the modulation amplitude as energy is increased. Some sources show double-humped pulse profiles. Thus models of accretion geometry should account for all of the observations above.

The simplest explanation for the existence of the double-humped pulse profiles is that the WD accretes from its both magnetic poles. Hellier (1999) proposes that the theoretical justification of two pole accretion is the non-existence of

magnetic monopoles and that, matter is attracted to both poles from the inner side of the accretion disk almost with the same force. Observational evidence for this is that the humps in the pulse profiles are almost 180^o out of phase. Another observational evidence proposed by Hellier (1999) states that fluxes of IPs never become zero at the spin minima contrary to polar systems.

King and Shaviv (1984) suggested that the quasi-sinusoidal variation of the light curves of IPs might be a geometrical effect and can be produced by a large polecap with a filling factor (defined to be the ratio of the area of the accreting region and area of the whole WD) more than 25%. According to the large polecap model, the maximum flux is detected when observing the accreting pole directly. This is because the X-ray emitting region (the polecap) is assumed to have a very small height, so a small optical thickness, and a large surface area in the radial direction where more X-rays can escape compared with the X-rays in the horizontal direction. Since the area covered by the polecap is high enough, the X-ray flux never goes to zero. We can, then, from this last sentence conclude that Hellier (1999)'s proposal may not be true (i.e. IP's fluxes never become zero is not an indication of two-pole accretion).

Pulse profiles can not be produced solely by a geometrical effect, since as we indicated above, the pulse profiles are energy dependent. Moreover, Kylafis and Lamb (1982) and Lamb (1988) showed that if the filling factor is on the order of 25%, then the height of the accretion column will be higher than the WD radius, which would yield much lower modulation depths since there would not be much occultation by the WD. Rosen (1992) found filling factors in the

range 0.1% to 2% if accretion is through a disk. All of these lead to the so called accretion curtain model (Rosen, Mason and Cordova 1988; Norton and Watson 1989; Rosen 1992, Hellier 1992). In this model, the natural magnetic field geometry of the WD is utilized which provides the accretion to occur in thin curtain like structures falling on the WD surface in arcs covering only 0.1-2% of the total WD surface. The energy-dependent mechanism causing the modulations in the X-ray and optical flux is the photoelectric absorption by the curtain. The cross-section for photoelectric absorption due to the ejection of electrons from the K-shell of atoms is given by

$$\sigma_K = \frac{9.7 \times 10^5 e^{12} m_e^{3/2} Z^5}{\pi^5 \epsilon_0^6 h^4 c} (h\omega)^{-3.5} \tag{2.4}$$

(Longair 1992), so the photoelectric absorption can account for the modulation depths of IPs decreasing with increasing energy. Up to now, no other energy-dependent mechanism except photoelectric absorption is found. Thus, it would be helpful in the understanding of accretion mechanism in IPs, to determine the exact form of the energy dependence, from the investigations of modulation changes of pulse profiles.

Table 2.1: Timing data for Intermediate Polars

Name	P (s) (s)	$\dot{P}$ 10^{-11}(s/s)	P_{orb} (hr)	Ref.
AE AQR	33.0767335(9) (1H, SB, QPO)	$5.642(20)\times10^{-3}$	9.87973(1)	1,2,3,4,5 6,7,8,9
V533 Her (N Her 1963)	63.633032(2)	<0.04	3.53	10,11,12
DQ Her	71.06540(1)	-0.05	4.646909(3)	13,14,15 16,17
XY Ari (H0253+193)	206.30(4)		6.0648(5)	17
V709 Cas	313		5.34(1)	18,19,20,21
GK Per	351.341(2) (1H, QPO)	-2.7	47.9233(2)	22,23,24 25,26,17
RX 0757+63	515		1.44	27
YY Dra (3A 1148+719)	529.22(8) (1H, SB)	<21	3.96(1)	19,28,29 30,31,32
V405 Aur	545(5)		4.15	27,33

(1) Patterson (1979a), (2) Feldth et al. (1980), (3) Patterson et al. (1980), (4) Jablonski (1981), (5) Chincarini et al. (1981), (6) Patterson et al. (1988), (7) Robinson et al. (1991), (8) de Jager (1991), (9) de Jager et al. (1994),(10) Patterson (1979b), (11) Hutchings (1987), (12) Thorstensen et al. (2000), (13) Balachandran et al. (1983), (14) Martell et al. (1995), (15) Zhang et al. (1995), (16) Silber et al. (1996), (17) Patterson (1994), (18) Cherepashchuk et al. (1996), (19) Norton et al. (1999), (20) Kozhevnikov (2001), (21) Bonnet-Bidaud et al. (2001), (22) Bianchini et al. (1981), (23) Crampton et al. (1986), (24) Watson et al. (1983), (25) Watson et al. (1985), (26) Norton et al. (1988), (27) Hellier (1999),(28) Mateo et al. (1991), (29) Patterson et al. (1992), (30) Patterson et al. (1993), (31) Reinsch et al. (1995), (32) Haswell et al. (1997), (33) Shakhovskoy et al. (2001)

Table 2.2: Timing data for Intermediate Polars

Name	P (s) (s)	$\dot{P}$ 10^{-11}(s/s)	P_{orb} (hr)	Ref.
V471 Tau	554.635(2) (1H, SB)		12.508397(2)	17,34,35
1WGA J1958.2+3232	733		4.36	67, 68
V1223 Sgr (4U 1849-31/3A 1851-312)	745.506(1) (SB)	+2.3(3)	3.36586(1)	36,37,38
AO Psc (H2252-035)	805.203(1) (SB)	-6.0	3.59105(4)	17,39,40 41,42
UU Col	864		3.45	27,43
RE 0751+144 (PQ Gem)	833.72(2) (SB)	+11	~5.6	44,45 46,47
BG CMi (3A 0729+103)	913.496(1) (SB)	-7.0	3.23397(2)	17,48
RX 1712-24			3.4: 27	

(34) Jensen (1985). (35) Robinson et al. (1988),(36) Warner B. et al. (1984). (37) Osborne et al. (1985), (38) van Amerongen et al. (1987) (39) Kubiak (1983), (40) Kubiak (1984), (41) Williams et al. (1984), (42) Schlegel (1999). (43) Burwitz V., Reinsch K., 1999, AGM, 15, C09 (44) Mason (1995), (45) Potter et al. (1997), (46) Mason (1997), (47) Stavroyiannopoulos et al. (1997) , (48) Singh et al. (1991). (67) Uslenghi et al. (2000), (68) Zharikov et al. (2001)

Table 2.3: Timing data for Intermediate Polars

Name	P (s) (s)	$\dot{P}$ 10^{-11}(s/s)	P_{orb} (hr)	Ref.
HZ Pup	1210		5.1	27
FO Aqr (H2215-086)	1254.451(1) (SB)	complex	4.849430(2)	49,50,51,52 53,54,55,56
RX 0153+74	1414			27
WX Pyx	1558			27
TV Col (2A 0526-328)	1910(4)		5.48641(1)	17,27
TX Col (H0542-407)	1911(10) (1H, SB)		~5.718	27,17,57
RX 1238-38	2147		1.41:	27
VZ Pyx (H0857-242)	2918(12)		1.78(9)	57,18,58
V1062 Tau (H0459+246)	3726(36)		9.95(7)	18,27
V603 Aql (N Aql 1918)	3780		3.3	27
EX Hya	4021.62(1)	-3.5	1.637612(1)	59,60,61,62,63
TW Pic (H0534-581)	7188(5)?		~6.2(1)?	64,65,66

(49) Berriman et al. (1986), (50) Pakull et al. (1987), (51) Shafter et al. (1987), (52) Patterson (1988), (53) Osborne et al. (1989), (54) Chiappetti et al. (1989), (55) Patterson et al. (1998), (56) Kruszewski et al. (1998), (57) Downes et al. (1993), (58) Thorstensen (1997) , (59) Mumford (1967), (60) Vogt et al. (1980), (61) Seetha (1987), (62) Heise (1987), (63) Ishida et al. (1994),(64) Mouchet et al. (1991), (65) Patterson et al.(1993), (66) Norton et al. (2000)

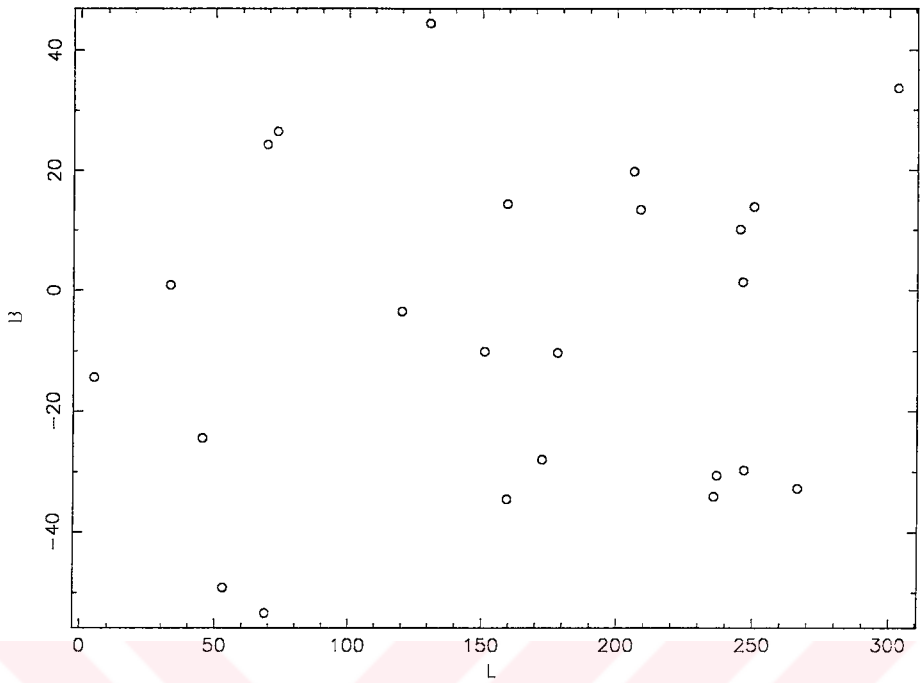


Figure 2.1: Galactic Distribution of Intermediate Polars

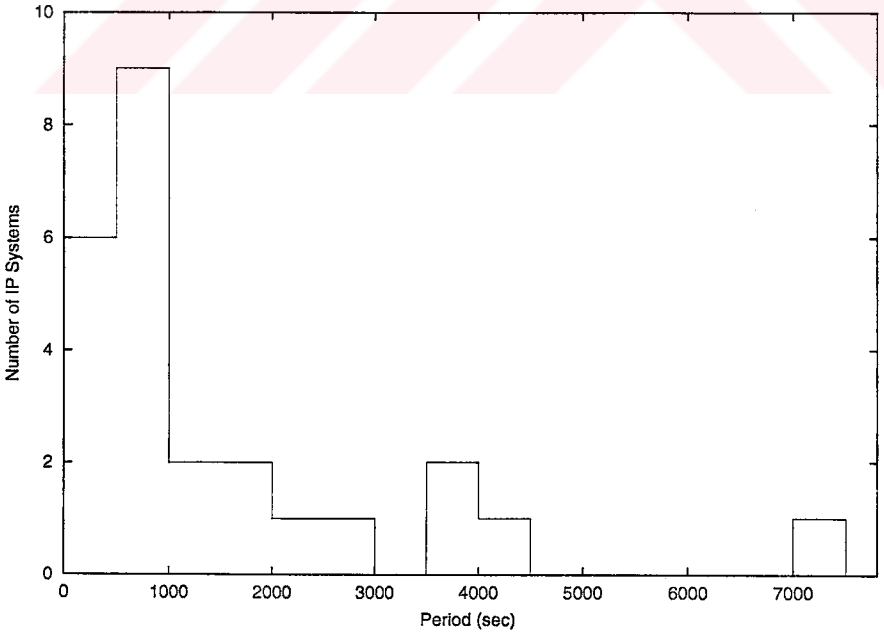


Figure 2.2: Spin Period Distribution of Intermediate Polars in 500 second bins

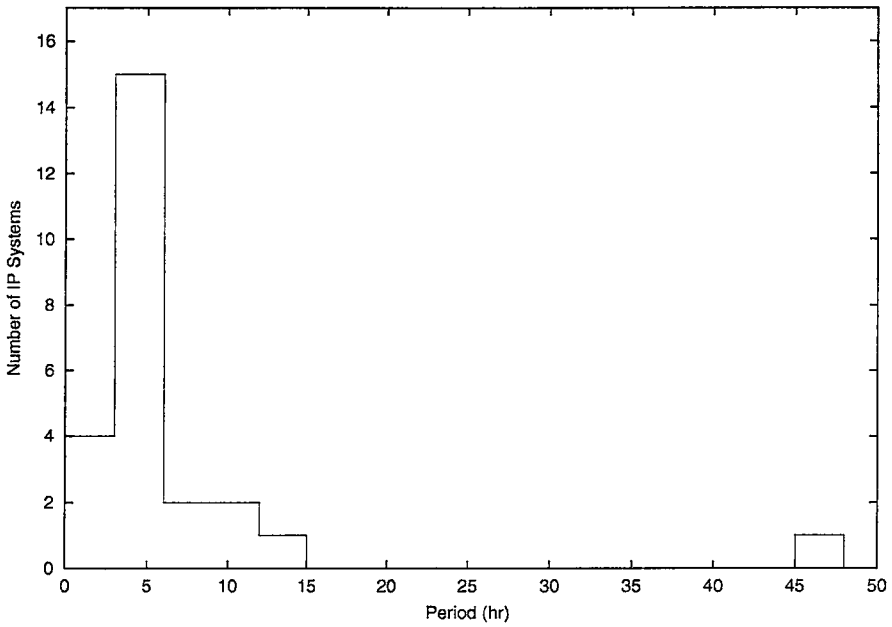


Figure 2.3: Orbital Period Distribution of Intermediate Polars in 3 hr bins

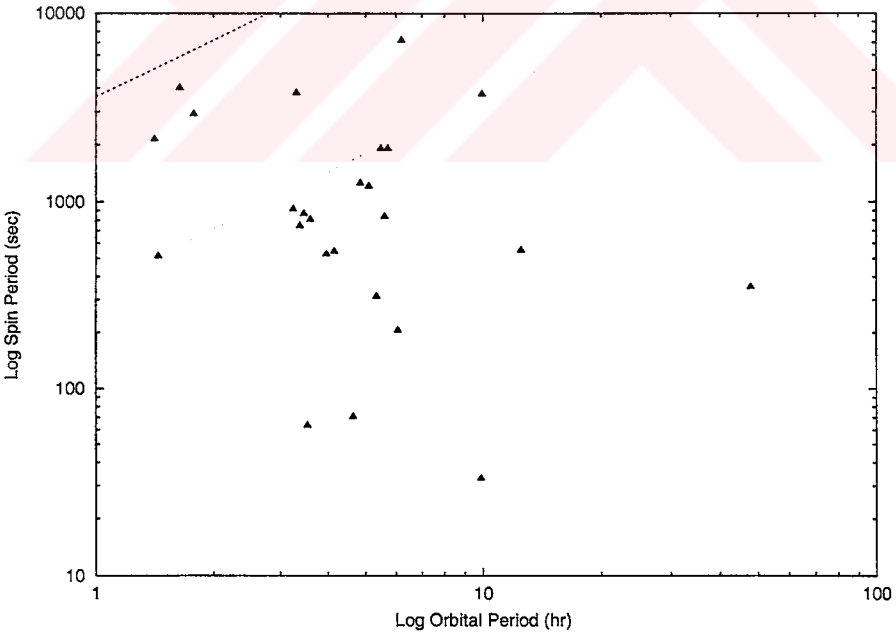


Figure 2.4: Spin Period vs. Orbital Period. The dashed line marks the region above which the spin period of an IP system becomes synchronized to the orbital period and the dotted line shows the relation $P_{spin} = 0.1 P_{orb}$

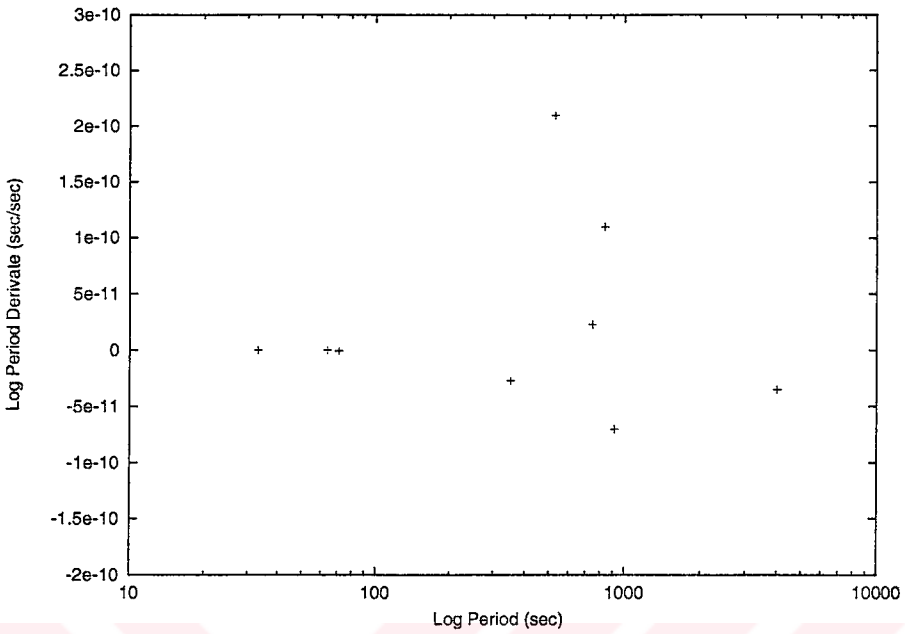


Figure 2.5: $P - \dot{P}$ Diagram for Intermediate Polars

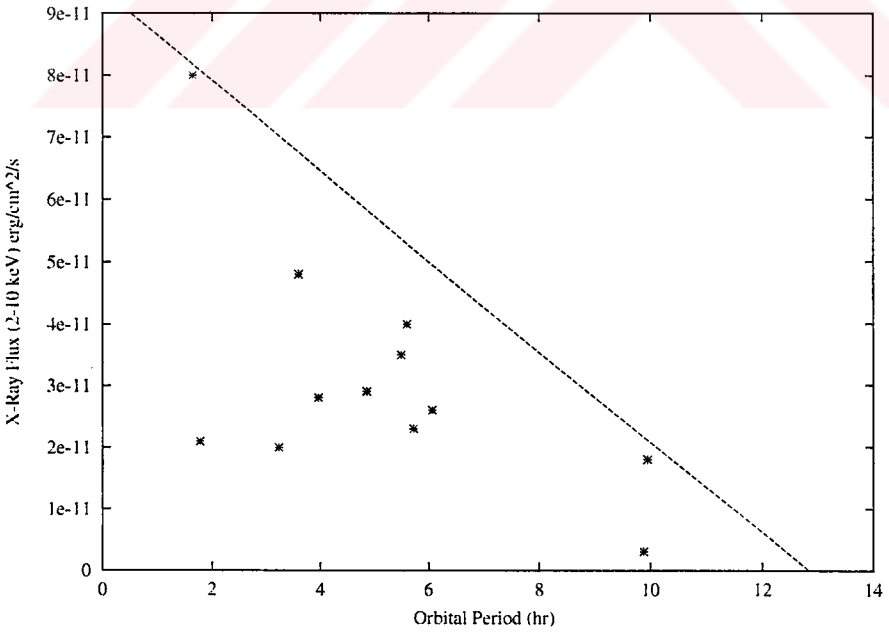


Figure 2.6: X-Ray Flux vs. Orbital Period

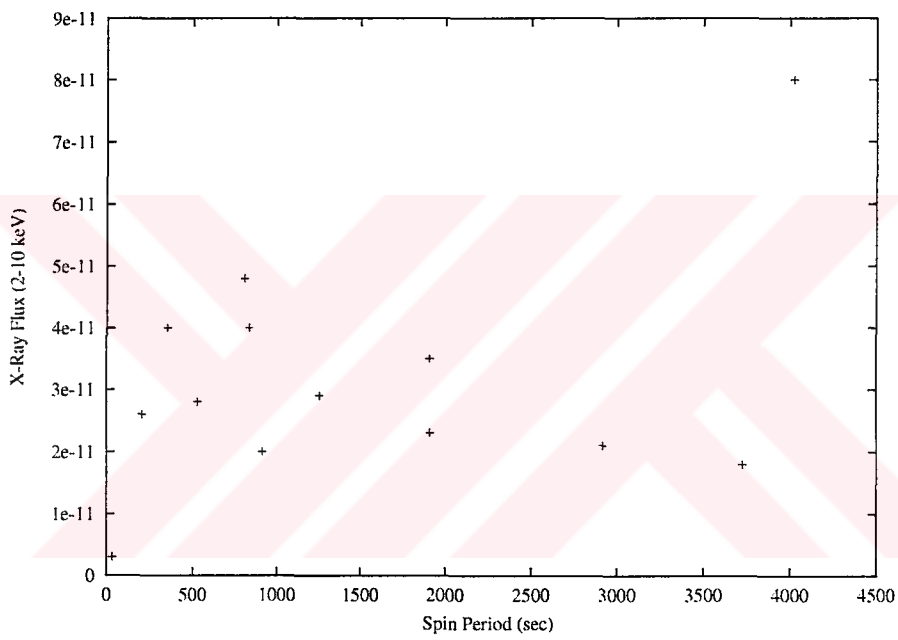


Figure 2.7: X-Ray Flux vs. Spin Period

CHAPTER 3

Power Spectral Methods for Astronomical Timing Analysis

3.1 Power Spectrum

3.1.1 Basic Definitions

Any arbitrary function can be constructed by adding an infinite number of sine and cosine functions with appropriate amplitudes by means of Fourier analysis and any signal can be decomposed into sine waves by a Fourier transform. In many of the experiments, the data is obtained in discrete units. Therefore, to obtain the Fourier transform of a signal, the discrete version of the transform (DFT) is used.

Assume that there are N data points, h_k (k=0,N-1), then the data h_k is decomposed into sine waves by the DFT as

$$a_j = \sum_{k=0}^{N-1} h_k exp(\frac{2\pi ijk}{N}) \qquad j = (-\frac{N}{2}, ..., \frac{N}{2} - 1) \tag{3.1}$$

$$h_k = \frac{1}{N} \sum_{j=\frac{N}{2}}^{\frac{N}{2}-1} a_j exp(\frac{-2\pi ijk}{N}) \qquad k = (0, ..., N-1) \tag{3.2}$$

a_j is the Fourier transform of the signal h_k. The DFT completely describes the signal h_k, but the highest frequency that can be used in this description is N

times the Nyquist frequency which is

$$\nu_{N/2} = \frac{1}{2T} \tag{3.3}$$

where T is the time-step. In our analysis, h_k represents the number of photons detected at time t_k. The error in frequency is the inverse of the total observation time. Note that

$$a_0 = \sum_k h_k = N_{ph} = \textit{ total number of photons} \tag{3.4}$$

The type of data we consider is composed of noise with a weak periodic signal. To detect this periodicity in the data, a power spectrum or a periodogram is used which is defined as (van der Klis, 1989):

$$P_j = \frac{1}{N_{ph}} |a_j|^2 \tag{3.5}$$

Thus, a power spectrum shows how strong the periodicity is at each frequency.

3.1.2 Statistics of the Power Spectrum

To obtain quantitative knowledge on the power of a source signal, the relation between noise and the signal power spectra must be known. In general, it is not possible to know this relation, but if the source signal is considered to be a small perturbation from the level of noise, then noise and signal powers can be considered as independent quantities. Thus, the total spectrum will be the superposition of the noise and the signal powers. In practice, the noise powers are χ^2 distributed for almost all types of noise (van der Klis 1989). The power spectrum definition given above is normalized such that if the input data were

pure Poissonian noise, then $P_{j,noise}$ is a χ^2 distribution with two degrees of freedom. Then the probability for a given $P_{j,noise}$ to exceed a $P_{threshold}$ is (van der Klis 1989):

$$Prob(P_{j,noise} > P_{threshold}) = Q(MWP_{threshold}|2MW) \tag{3.6}$$

$$Q(\chi^2|\nu) = 2^{-\nu/2}\Gamma(\nu/2)^{-1}\int_{\chi^2}^{\infty} t^{\frac{\nu}{2}-1}exp(-t/2)dt \tag{3.7}$$

$P_{threshold}$ represents the minimum level at which a signal is significant corresponding to a given confidence level; ν is the number of degrees of freedom; W is the number of frequency bins used in the Fourier transform and M is the number of data set segments in which all the segments should span equal times; and Γ is the gamma-function. Following these definitions the detection level is:

$$\frac{\epsilon}{N_{trial}} = Q(MWP_{detect}|2MW) \tag{3.8}$$

with $100 \times (1-\epsilon)$ percent confidence. Thus ϵ can be considered as a false alarm probability. N_{trial} is the number of P_j to compare with P_{detect}. In Figure 3.1. P_{detect} is plotted as a function of N_{trial} for different MWs.

3.2 Lomb-Scargle Periodogram Analysis

3.2.1 Definition

A powerful method to detect weak periodic signals in a noisy background was developed by Lomb (1976) and Scargle (1982) for unevenly sampled data. The method is valuable for analysis of uncontrolled experiments like astronomical observations which cannot control the arrival times of the photons to be detected.

The Lomb-Scargle method is a new definition of the periodogram in which the periodogram is the same as least squares fitting of sine waves to the data at a frequency ω, so that the statistical properties are easy to evaluate. Least squares fitting is in the form

$$h(t) = Acos(\omega t) + Bsin(\omega t) \tag{3.9}$$

If we have a time series h_i, i=1,.....,N (h_i again is the number of photons in bin i), then the Lomb-Scargle periodogram is defined as

$$P_N(\omega) = \frac{1}{2\sigma^2}\frac{[\sum_j (h_j - \bar{h})cos\omega(t_i - \tau)]^2}{\sum_j cos^2\omega(t_i - \tau)} + \frac{1}{2\sigma^2}\frac{[\sum_j (h_j - \bar{h})sin\omega(t_i - \tau)]^2}{\sum_j sin^2\omega(t_i - \tau)} \tag{3.10}$$

where $\bar{h} = \frac{1}{N}\sum_1^N h_i$ is the mean and $\sigma^2 = \frac{1}{N-1}\sum_1 N(h_i - \bar{h})^2$ is the variance. The variable τ makes the periodogram time-translation invariant and it is defined by

$$\tau = \frac{1}{2\omega} arctan \frac{\sum_j sin2\omega t_j}{\sum_j cos2\omega t_j} \tag{3.11}$$

3.2.2 Statistics and Computation

When a peak is found in the periodogram, the significance of the peak must be calculated. Scargle (1982) showed that with the normalization adopted above by σ^2, assuming that the data are independent Gaussian random values, the false alarm probability of any peak in $P_N(\omega)$ when M independent frequencies are searched is

$$P(> z) = 1 - (1 - e^{-z})^M. \tag{3.12}$$

The false alarm probabilities give the significance levels. Significance level is (1-false alarm probability). Since we are interested in small false alarm probabilities,

Eq.3.12 can be expanded in a binomial series, and the first term gives

$$P(> z) \approx Me^{-z} \tag{3.13}$$

This equation shows that as number of frequency trials increases, the significance of any peak in the spectrum decreases almost linearly. In fact, for the general case of unevenly sample data, M is not equal to the number of frequency trials. It also depends on the number of data points and the spacing between each data point. The best way to determine M for a given data set is to use a Monte Carlo method. Results of some Monte Carlo computations for various cases are given in Horne and Baliunas (1986). Also there is another computation method more practical but less accurate given in Press et al. (1996).

The computer must perform $4N^2$ multiplications to calculate the Lomb-Scargle periodogram and this takes about 4 days for 20000 data points on a high performance personel computer. The periodogram cannot be calculated directly by the use of fast fourier transform, because the data points are unevenly sampled. But there is an indirect method developed by Press and Rybicki (1989) which uses a method based on interpolation and extirpolation (inverse interpolation). In this method, first a curve is fitted to the data by interpolation and then the curve is extirpolated to give an evenly spaced data set. Then the data can be transformed by using fast Fourier transform (FFT), since the data is now evenly spaced. Interpolating and then extirpolating the data, increases the error in the data to be transformed. Thus the calculation of period and period derivatives using DFT is more favorable even though it has more complicated statistical

properties compared to Lomb-Scargle method. However, for cases where there is a small data set or a very fast computer or the period is known before-hand, the Lomb-Scargle method would give more trustworty results.

3.3 Fast Fourier Transform (FFT)

FFT is an efficient method for calculating the DFT. It requires only on the order of $Nlog_2N$ multiplications to calculate DFT. If a complex number $W = exp(2\pi i/N)$ is defined, then Eq.3.1 becomes

$$a_j = \sum_{k=0}^{N-1} W^{nk} h_k. \tag{3.14}$$

FFT uses the fact that a DFT of length N can be written as a sum of DFT's of length N/2. This is done by seperating the odd and even indexed points of the transform;

$$F_k = \sum_{j=0}^{N-1} e^{2\pi ijk/N} f_j = \sum_{j=0}^{\frac{N}{2}-1} e^{2\pi ijk/(N/2)} f_{2j} + W^k \sum_{j=0}^{\frac{N}{2}-1} e^{2\pi ijk/(N/2)} f_{2j+1} = F_k^e + W^k F_k^o. \tag{3.15}$$

If N is a power of 2, this procedure can be performed until the original DFT can be written in terms of DFTs of length one. Then one component of the DFT becomes

$$F_k^{eoeeoeoo...eoee} = f_n \tag{3.16}$$

This means that for every input number f_n, there is a corresponding one-point transform. Then the corresponding pattern of e's and o's for every n must be determined. The recipe is first reverse the pattern of e's and o's, then write e=0 and o=1, and then the pattern becomes the value of n in binary mode. This method

is called bit-reversal. If the original data points are arranged by bit-reversal, then the data points become one-point transforms. After that, combining every neighbouring points, we get the two-point transforms, then combining them we get the 4-point transforms, and so on. By this recursive method the DFT is calculated.

The separation of the DFT into even and odd components requires $log_2 N$ arithmetical operations and the addition of the one-point, two-point, etc. requires N operations. So a complete DFT can be calculated by $Nlog_2 N$ operations.

Codes of FFT can be found in Press et al. (1996) and Brigham (1974).

3.4 Cross-Correlation

The cross-correlation function represents the correlation between two similar functions at different times, locations, etc. The discrete correlation of two functions g and h is given by (Press et al., 1996):

$$Corr_{g,h}(t_j) = \sum_{k=0}^{N-1} g(t_{j+k}) h_k \tag{3.17}$$

here, k represents the lag. The correlation will give a large value if the function g is very similar to h with a time lag of t_k. In our case, the correlation function can be used to give the phase difference between two light curves. To calculate the correlation function, the discrete correlation theorem is utilized,

$$Fourier\ transform\ of\ Corr_{g,h}(t_j) = G_k H_k^* \tag{3.18}$$

where G_k and H_k are the Fourier transforms of g_j and h_j and the asterix is the complex conjugate sign. First the Fourier transforms of each data set is calculated

and then each term in a set is multiplied with the corresponding term in the other set. Finally taking the inverse Fourier transform will yield the correlation between the two functions. Cross correlation is especially useful in determining period derivatives and calculation and simulation of noise parameters of time-series data.

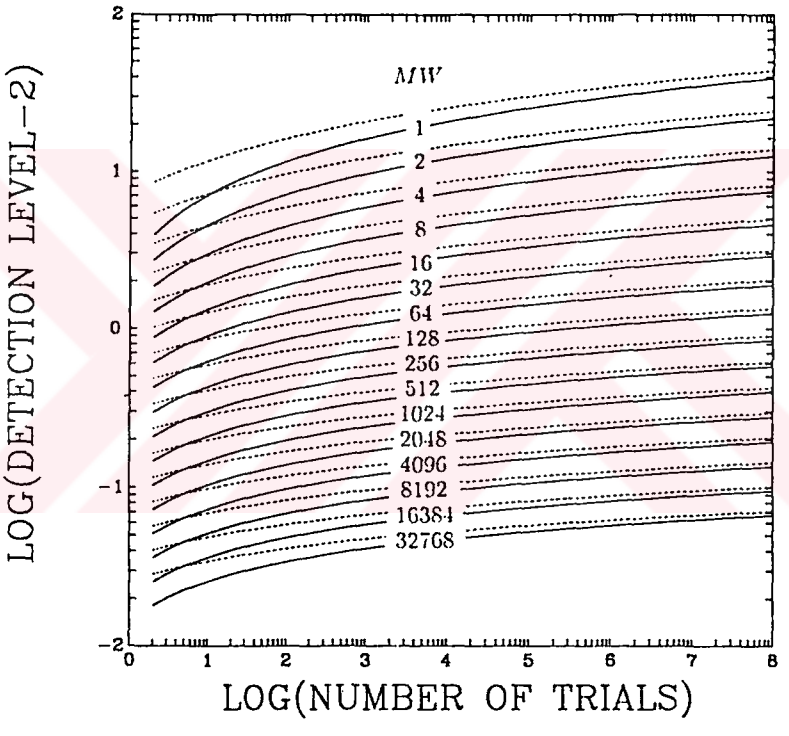


Figure 3.1: 99% (dashed lines) and 90% (solid lines) confidence levels. From van der Klis, 1989

CHAPTER 4

ROSAT Timing Analysis of AE Aquarii

4.1 AE Aquarii

AE Aqr is a nova-like variable 90 pc away with a visual magnitude of $V \sim 11 - 14$. The X-ray flux of the source is $F_x = 0.3 \times 10^{-11}$ erg cm^{-2} s^{-1} in the 2-10 keV band. It is a unique member of the IP class and has the shortest spin-period among known IPs. It also displays propeller properties (Eracleous 1999). The spin period ($\sim$ 33 s) is detected in the range from optical to gamma ray frequencies with ground based and satellite observations (Patterson 1979; Meintjes et al. 1992; Eracleous et al. 1991). Along with the spin period of $\sim$ 33 s, also the first harmonic of this pulse is detected with considerable power (much higher than 99% confidence level) and an orbital sideband is found (our work). The spectroscopic and photometric studies have shown that the orbital period of the binary system is $\sim$ 9.88 hrs. AE Aqr shows rapid flaring activity in the optical band and it emits strong pulsed TeV gamma rays during these flares (Meintjes et al. 1992). The flaring activity and emission of gamma rays are not common in IPs.

4.2 Data Analysis

4.2.1 Spin-Period of the White Dwarf in AE Aquarii

Three sets of archival ROSAT data were obtained with the position sensitive proportional counter (PSPC). The data are analyzed with the MIDAS/EXSAS Software Package (Zimmermann et al. 1994). The three sets of data were taken between April-25 and May-11 1991 with an effective exposure of 3075 s; November 10 and 16, 1992 with an effective exposure of 20662 s, and October 20 and 21, 1993 with an effective exposure 6922 s. The power spectrum of the November 1992 data derived from a DFT analysis is shown in Figure 4.1. In this figure, three prominent peaks are seen. The central peak is the real period of the WD. The solid line parallel to frequency-axis in Figure 4.1 shows the detection threshold power corresponding to 99% confidence level. The other two peaks near the central peak in Figure 4.1 are found to be caused by the rotation of the satellite with a period of 90 min. Thus, the spin period of the WD is confirmed to be 33.079(2) s. The power spectrum shown in Figure 4.2 is for the October 1993 data. The period detected is the same in Figure 4.1 but with less power because the total observation time is shorter. However, the peak is over the detection threshold.

The data is also analyzed by folding the time series around the expected periods using EXSAS/MIDAS software. In this analysis, the software gives the deviation of the fitted model (indicated by χ^2) at the given period from a random distribution. To have a strong signal χ^2/N_{pb} must be higher than 1 (N_{pb} represents

the number of phase bins in the pulse profile, which is 20 for our work). For the data with 20662 s effective exposure, it is found that the spin period is 33.0767335 s with χ^2/N_{pb}=7.025. The most powerful signal is found at 33.076755 s with χ^2/N_{pb}=7.425. For the data with 6922 effective exposure, we have found that the spin period at 33.0767335 s have χ^2/N_{pb}=4.255. Also a period around 33.10745493 s is found with χ^2/N_{pb}=2.7375, corresponding to sideband $\omega - \Omega$.

We have also prepared Lomb-Scargle and DFT codes using Fortran 77. In the first data set no periodicity is found. In the second and third data sets, periods close to 33 s are found which are above the detection thresholds. No considerable difference is found between using DFT or the Lomb-Scargle Method, in our results.

4.2.2 Pulse-Profiles of AE Aquarii

We have constructed pulse profiles folding the data sets on the periodicity found in the first (in time) data set in time which has a frequency of 0.030230(2) Hz. The pulse profiles are displayed in Figures 4.3 and 4.4. By the comparison of the pulses in the two Figures, we find that there is phase shift of $\sim$ 0.4 s (same value is found by a cross correlation analysis). This may indicate a change of period or change in the accretion geometry. If we assume a constant $\dot{P}$ and also assume that the phase shift of the pulse profiles are only due to a period change, the phase shift can be represented by

$$\Delta\phi = \frac{1}{2}\dot{\nu}t^2 + \frac{1}{6}\ddot{\nu}t^3 + ... \tag{4.1}$$

where $\Delta\phi$ is the phase shift of the pulse profiles in time t, and $\dot{\nu}$ is the frequency change in time. This yields a $\dot{P}$ of $\sim 1\times10^{-12}$ s/s. This is two orders of magnitude higher than the unambiguosly measured $\dot{P}$ of AE Aqr by phase connected optical pulses. Our data set is not continuous enough to have phase connection between the pulses. Thus, we cannot conclude if this phase shift comes from a period change or an accretion geometry change. We have also constructed pulse profiles of YY Dra using ROSAT and ASCA data sets spanning 6 years. We have found phase shifts similar to that of AE Aqr. However, that the errors are large on pulse profiles and the separation of consequent data sets are too large to determine $\dot{P}$.

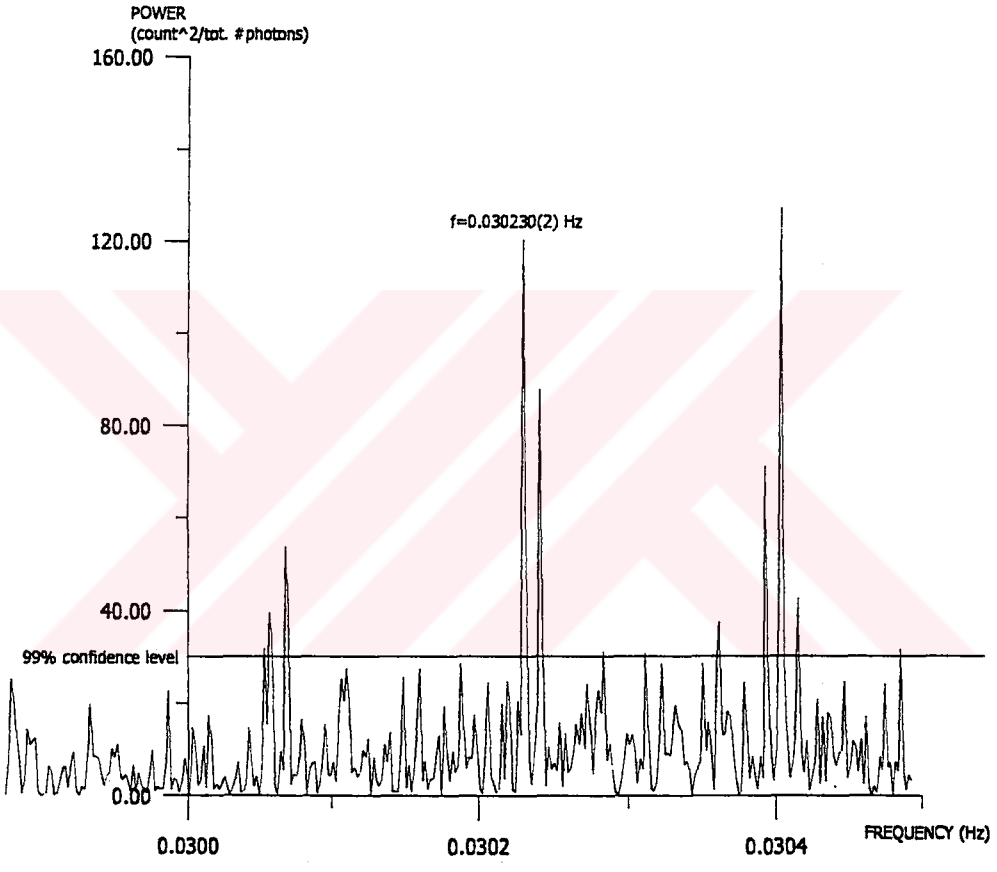


Figure 4.1: Power Spectrum of AE Aqr from the ROSAT observation in 10-16 November 1992

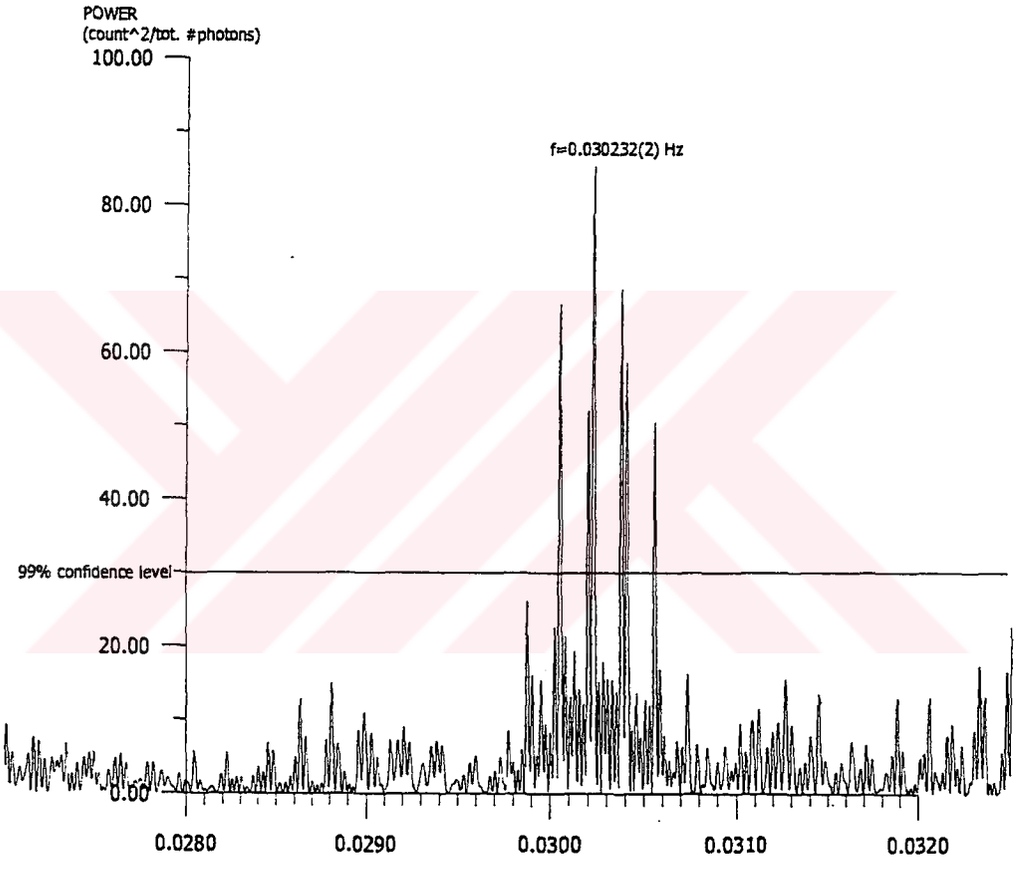


Figure 4.2: Power Spectrum of AE Aqr from the ROSAT observation in 20-21 October 1993

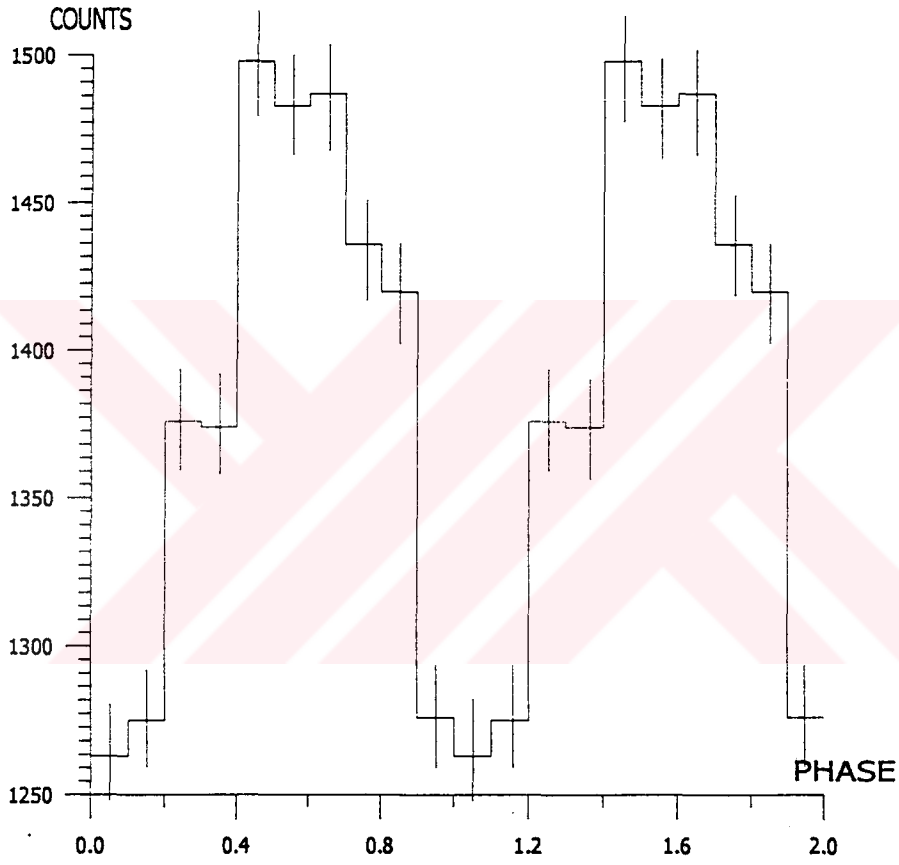


Figure 4.3: Pulse Shapes of ROSAT data of AE AQR taken between 10-16 November 1992

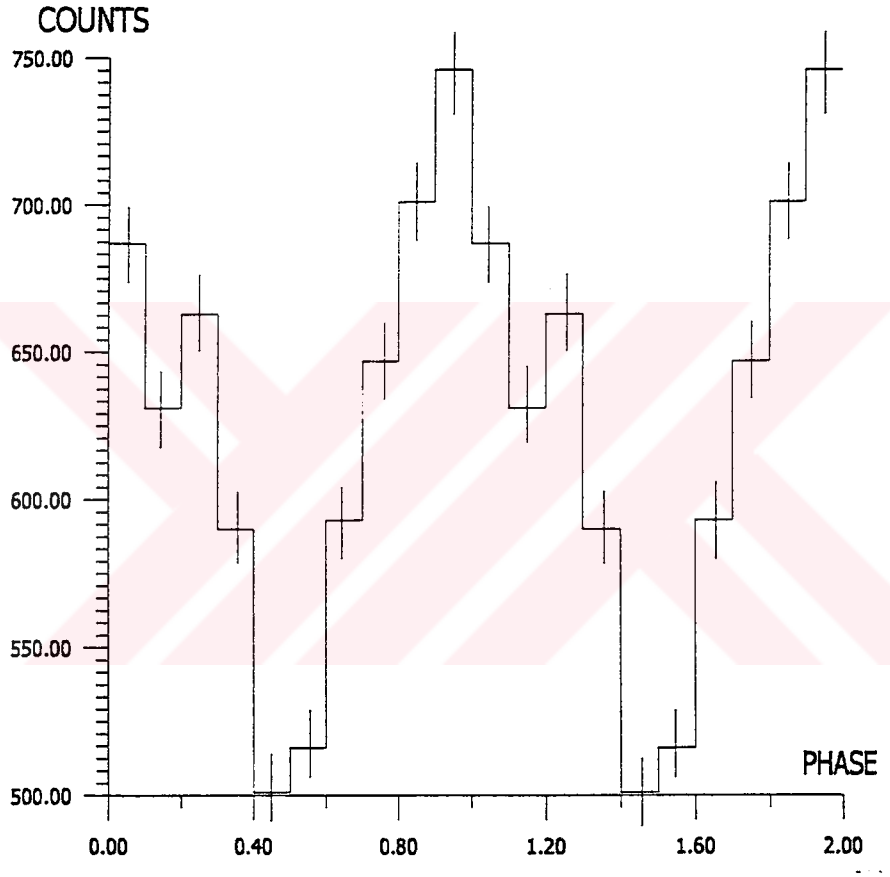


Figure 4.4: Pulse Shapes of ROSAT PSPC data of AE AQR taken between 20-21 October 1993

CHAPTER 5

Spectral and Temporal Analysis of the Intermediate Polar YY Dra in the Energy Range 0.1-10 keV

5.1 Introduction

YY Dra is a 16th magnitude IP which has short dwarf nova outbursts (Wenzel, 1983). It has an orbital period of 3.97 hours detected in the optical (Haswell et al. 1997 and Friend et al. 1988) and infrared (Mateo et al. 1991) wavelengths. Patterson et al. (1992) discovered periodicities in the light curve of YY DRA at 265, 275 and 550 seconds by optical photometry. Using ROSAT PSPC data Patterson and Szkody (1993) found a period of 264.6 s which was half the period Beuermann and Thomas (1993) and Reinsch et al. (1995) published using the ROSAT All Sky Survey (RASS) data. Also, Reinsch et al. (1995) claimed the existence of a period of 530.9 s which was also found using the ROSAT PSPC data obtained in 1993. The existence of the period around 530 seconds and 265 seconds led to the conclusion that the true rotation period of the WD was 529.22 s and the 550 s periodicity was the orbital sideband of the WD revolution period.

Reinsch et al. (1995) found switching pulse profiles between single and double-peaked shapes, using three consecutive ROSAT data sets in October 1990. These results led the authors to conclude that YY Dra usually accretes on to both of its poles and sometimes only to one pole. Haswell et al. (1997) strengthened the two-pole accretor model by showing the existence of 529.31 s, 264.71 s and 273 s periodicities with the Hubble Space Telescope spectroscopic data. Moreover, Norton et al. (1999) detected a period at 264.7 s from ROSAT HRI data obtained in 1996, and found that the X-ray pulse profile shows double humps when folded on the spin period of the WD. Finally, Szkody et al. (2002) have found that the spin pulse modulation decreases considerably during the outburst compared with the quiescent stage using the RXTE data obtained in 1999 September (quiescence) and in 2000 November (outburst).

The EINSTEIN X-ray spectrum of YY Dra modeled as a thermal bremsstrahlung (see 5.4.1) emission yielded a temperature higher than 4.4 keV , $N_H < 0.36 \times 10^{21}$ cm^{-2} and F_x(0.1-3.5 keV)=$0.90^{+0.09}_{-0.10} \times 10^{-11}$ erg cm^{-2} s^{-1} with a reduced χ^2 of 3.93 (Eracleous et al. 1991). Using ROSAT PSPC data, Richman (1996) found the best fitting thermal bremsstrahlung parameters as, kT=1.5$\pm$0.2 keV, N_H= 2.0 $\pm$0.2 $\times$ 10^{20} cm^{-2} and F_x(0.1-2.4 keV)=7.70×10^{-12} erg cm^{-2} s^{-1}, but with a reduced χ^2 of 8. Richman (1996) noted that the fits do not improve by applying a two-temperature bremsstrahlung model. Furthermore, Szkody et al. (2002) modeled the RXTE spectrum by absorbed single bremsstrahlung and Raymond-Smith models (see 5.4.1). They have also found that adding other temperature components did not yield a better description of the spectrum.

5.2 Observations and Data

The archival ASCA observation of YY Dra was conducted on 1997 May 6 with the Gas Imaging Spectrometer (GIS) (Makishima et al. 1996 ; Ohashi et al. 1996) working in the range 0.7-10 keV and Solid-state Imaging Spectrometers (SIS) working in the 0.4-10 keV energy range (Burke et al. 1991 ; Yamashita et al. 1997). SIS has an energy resolution of $\Delta E/E = 0.02$ at 5.9 keV. GIS is a gas scintillation proportional counter with high timing resolution and a spectral resolution four times lower than the SIS. SIS is more sensitive in relatively lower energies down to 0.4 keV and GIS is more sensitive in higher energies, up to 10 keV.

The source was observed with an exposure of $\sim$ 24.4 ks with GIS and $\sim$ 32.9 ks with SIS. The background subtracted count rate is found to be $\sim$ 0.3 cts s^{-1} for both GIS and SIS observations. For timing analysis, we have used pulse-height normal mode (PH normal mode) data of the GIS detectors, and for spectral analysis, we have used bright2 medium bit-rate data of the SIS detectors. In order to extract source photons, we have used a circular aperture with radii 3 and 2 arc minutes for GIS and SIS observations, respectively. The background is selected from an annular region around the source having approximately the same area as the source extraction radius. In screening the data, standard data selection criteria was assumed. The fits to the data were performed using spectral analysis package XSPEC (v.11).

5.3 Temporal Analysis

To investigate the timing behavior of YY Dra, the photon arrival times are corrected to the solar system barycenter. The background-subtracted GIS light curve integrated into 100-s bins is displayed in Figure 5.1. We have performed a discrete Fourier transform on the light curve and found a signal at 264.9±9.0 s and also at 526.3±3.5 s. The power spectrum is displayed in Figure 5.2. The 529.22 s periodicity quoted by other authors is within the error bar of the 526.3 s signal. We note that both signals are detected at the same power.

We have also investigated the energy dependence of the pulse profiles. After subtraction of the background, we have divided 10-s binned GIS3 data into two different energy bands with approximately equal count rates. First energy band is between 0.7-2 keV (corresponding to channels 60-165) with 0.136(3) cts s^{-1} and the second energy band is between 2-10 keV (corresponding to channels 165-850) with 0.142(3) cts s^{-1}. We have folded the two light curves on the 264.6 seconds and 529.2 seconds periodicities (Figure 5.3). The overall peak to peak modulation depth was determined using the definition $100\times(I_{max} - I_{min})/I_{min}$; where I_{max} and I_{min} are maximum and minimum count rates in the best fitting sinusoid. The modulation depth of the 264.6 s signal in 0.7-2 keV band is 11.8±6.2 %, and the modulation depth of the same signal in 2-10 keV band is 44.6±6.6 %. The uncertainties quoted above for modulation depths are 1σ errors. The difference of modulation depths in the two energy bands is 32.8±9.1 % at 1σ. This shows that modulation depth of X-ray pulses of YY Dra increase as energy is increased in the

2-10 keV energy band. This is consistent at more than 3σ confidence level when 3σ errors on both pulse profiles are propagated to calculate the error on the difference of the modulation depths in the two consecutive energy bands. The light curve folded on 529.2 s shows a double peaked structure both in the total energy band and in the 2-10 keV band (Figure 5.4). Moreover, the 0.7-2 keV profile is almost flat-topped. Because of the above reasons, to determine the modulation depths, we did not fit sinusoidal functions to the pulse profiles, instead we have taken I_{max} and I_{min} as the maximum and minimum count rates in the pulse profiles, and we have used the definition of the modulation depth given above. Then the modulation depth in 0.7-2 keV band is $\sim$42 % and in the 2-10 keV band the modulation depth is $\sim$56 %. We note that these approximate modulation depths are not as trustworthy as the ones determined for the light curve folded on 264.6-s. because of the complex structure of the pulse profile of 529.2-s signal. We have followed the same procedures to determine the modulation depths with GIS2. The results are similar with the ones obtained for GIS3. However the pulse amplitudes obtained from the GIS2 data are slightly lower than the ones obtained from GIS3 data. This is due to fact that GIS2 detector has a lower energy resolution than GIS3 detecor, also GIS2 has a higher background. We have also investigated the energy dependence of the pulse profiles by combining GIS2 and GIS3 and again found similar modulation depths which increase as energy is increased. We also want to note that there are shape and phase differences in the pulse profiles between the different energy bands and different folding periods (Figure 5.3 and 5.4).

5.4 X-Ray Spectra

5.4.1 Spectral Models

The spectrum of IPs are generally modelled by thermal bremsstrahlung (Kellogg et al. 1975) and Raymond-Smith (Raymond and Smith 1977) models. The spectrum of thermal bremsstrahlung from an optically thin thermal plasma is given by

$$F(E) = A_{tb} e^{-E/kT} (E/E_0)^{-1} g(E;kT) \tag{5.1}$$

where $A_{tb} = (3.02 \times 10^{-15}/(4\pi D^2)) \int n_e n_H dV$ in cm^{-2} s^{-1} keV^{-1} is the normalization constant, k is the Boltzmann constant, g(E;kT) is the Gaunt factor, D is the distance to the source and n_e and n_H are the electron and ion densities respectively in cm^{-3}.

Raymond-Smith model represents a thermal plasma which has spectrum

$$F(E) = A_{rs} \Lambda(E,T) \tag{5.2}$$

where A_{rs} is the normalization constant which is equal to $10^{-14}/4\pi D^2 \int n_e n_H dV$ in cm^{-5}, D is the distance to the source and Λ(E,T) is the cooling function.

Now, there are other models to model the complicated X-ray spectrum of IPs such as MEKAL, VMEKAL, c6VMEKAL (Mewe et al. 1985, Mewe et al. 1986, Kaastra 1992), ABSORI (Zdziarski et al. 1995), HREFL (Done et al. 1995) and PCFABS (Ezuka and Ishida 1999). MEKAL/VMEKAL/c6VMEKAL models are the same as the Raymond-Smith model. however the spectrum includes C,N,O,Ne,Na,Mg,Al,Si,S,Ar,Ca,Fe,Ni abundances. For MEKAL model

solar abundances are assumed, and for the VMEKAL model abundances are variable. c6VMEKAL model is the same as MEKAL model but with multi-temperatures. This model uses 6-order Chebyshev polynomial for the differential emission measure.

ABSORI is an ionized absorber model with variable iron abundance. The spectrum depends on power law index, hydrogen column density, absorber temperature and absorber ionization state.

HREFL model gives the spectrum of the reflected X-rays from a cold, optically thick, circular slab with inner and outer radii illuminated by a point source a height H above the centre of the slab. Spectrum depends on angle between source photons incident on the slab and the slab normal, angle between the observer's line of sight and the slab normal, iron abundance, iron K-edge energy and fraction of the direct flux seen by the observer.

PCFABS is a partial covering fraction absorption model for the accretion column of CVs. This model includes the relative abundances. The spectrum is given by

$$F(E) = Ce^{(-N_{H,ave}\sigma(E))} + (1 - C) \tag{5.3}$$

where σ(E) is the photo-electric cross-section without Thompson scattering, C is the covering fraction defined to lie between 0 and 1, and $N_{H,ave}$ is the average hydrogen column density in units of 10^{22} cm^{-2}.

5.4.2 Spectra of YY Dra

For spectral analysis, we have used only the SIS data because the GIS data was obtained with a lower energy resolution. We have combined SIS0 and SIS1 data and binned the spectrum to get a minimum of 40 photons in each energy bin. We have ignored the channels in the very low and very high energy ranges of the spectrum where the detector response was poor. In general, the spectrum of IPs are consistent with a single or two-temperature bremsstrahlung, VMEKAL or MEKAL models (Mewe, Gronenschild and van den Oord 1985; Kaastra 1992), with a photo-electric absorption or partial covering absorber model (Ezuka and Ishida 1999 and references therein).

In our analysis, we found that a single-temperature as well as two-temperature bremsstrahlung or VMEKAL/MEKAL models fit the ASCA spectrum of YY Dra with $\chi^2_\nu \sim 0.9$. In Figure 5.5, the combined ASCA SIS spectrum fitted with a single-temperature VMEKAL model is displayed and the spectral parameters of the fitted models are tabulated in Table 5.1. We have also tried to find an evidence for a partial covering absorber, however all of the fits yielded covering fractions of 99%, indicating that there is almost no partial covering absorber in the accreting region. In Figure 5.5, it is evident that a weak iron emission line exists near $\sim$7 keV. The upper limit to the iron abundance compared to the Solar iron abundance is <1. There are also excess humps in the spectrum near 1 keV indicating evidence for Fe L-shell emission lines (significance does not exceed 2σ).

The total unabsorbed X-ray flux inferred from single-temperature bremsstrahlung

model is $F_x^{unabs} = 1.8^{+0.2}_{-0.3} \times 10^{-11}$ erg cm^{-2} s^{-1} in 0.5-10 keV band, and the absorbed X-ray flux in the same energy band is $F_x = 1.7^{+0.4}_{-0.1} \times 10^{-11}$ erg cm^{-2} s^{-1}. The unabsorbed X-ray flux translates to an X-ray luminosity of $L_x = 5.2^{+0.6}_{-0.9} \times 10^{31}$ erg s^{-1}, if we assume a distance of 155 pc (Patterson 1994). The normalization parameter for thermal bremsstrahlung model is defined by norm=$(3.02 \times 10^{-15}/(4\pi D^2)) \int n_e n_h dV$ cm^{-5}; where D is the distance to the source in cm, n_e and n_H are the electron and neutral hydrogen column densities in cm^{-3}, V is the volume in which the photons emerge and the quantity $\int n_e n_H$dV is the emission measure (EM). Utilizing this formula, EM is calculated to be 3.5×10^{54} cm^{-3}. The typical length scale of the accretion column in IPs is $\sim 5 \times 10^7$ cm (Cropper et al. 1998). Assuming a base radius of $\sim 5 \times 10^7$ cm and a height of $\sim 10^8$ cm for a cylindrical accretion column, the electron density is found to be $n_e \approx 2.1 \times 10^{15}$ cm^{-3} (the electron and ion densities are assumed to be equal). The accretion rate of YY Dra is estimated to be $\dot{M} \approx 2.2 \times 10^{14}$ gr s^{-1} using the relation $\dot{M} \approx LR/GM$ (L is the luminosity in erg s^{-1}; R is the radius of the WD taken to be $0.008 R_\odot$; M is the mass of the WD in gr taken to be $1.0 M_\odot$ and G is the universal gravitational constant). The neutral hydrogen column density and bremsstrahlung temperature for YY Dra is lower compared with the values for most of the other IPs (eg. Ezuka and Ishida, 1999). However, the high temperature components determined from fits with two-temperature models are similar to the temperatures that are found for other IPs. The neutral hydrogen column density in YY Dra is considerably low by a factor of 10-100. These show that YY Dra has extreme characteristics.

5.5 Discussion

5.5.1 The X-ray Pulse Profiles

Some previous X-ray observations of other IPs show that modulation depth of pulse profiles decreases with increasing energy (Norton and Watson 1989; Shafter, Szkody and Thorstensen 1986, Mason et al. 1992, Haberl et al. 1994), which is explained by photo-electric absorption in the accretion column or curtain. Norton et al. (1999) proposed. for YY Dra and other fast rotating IPs, that the accretion scale height should be low due to the small value of the magnetic field of the WDs in these systems. This may cause the footprint of the accretion column to be large which, in turn causes the side-view optical depth in the accretion column to be lower than the face-on optical depth (Norton et al. 1999, Hellier 1999). In this scenario. the energy dependence of the modulations are caused by the photo-electric optical depth which decreases as the energy of the incoming photon increases. Thus. as the energy is increased, the optical depth difference between side-view and face-on view decreases diminishing the pulse amplitude.

Our results based on the ASCA data of YY Dra show that the modulation depth of the X-ray pulse profiles increases with increasing energy in the 0.5-10 keV energy range. Thus, the post-shock environment of YY Dra is somewhat more unique compared with its own kind and the modulation prescription described above is inadequate in explaining how the pulses are produced in YY Dra. Also, recent data from RXTE show evidence that, in some other MCVs, modulation depth increases with increasing energy (Mukai 2001. private communication).

To study the characteristics of the X-ray pulse profiles of YY Dra at lower energies (e.g., looking for evidence on modulation due to photo-electric absorption), we have analyzed the 22-25 May 1996 ROSAT archival data of YY Dra obtained by the High Resolution Imager (HRI) (Zombeck et al. 1995). The total exposure time of this observation is $\sim$ 56 ks which is the longest of the ROSAT observations of YY Dra. The mean background-subtracted count-rate is $\sim$ 0.3 cts s^{-1}. We analyzed the pulse profiles in $\sim$ 0.1-1.0 keV and $\sim$ 1.0-2.0 keV energy ranges with similar count-rates in the two energy bands, $\sim$ 0.15 cts s^{-1}, consistent with the count-rates we have used in the ASCA pulse profile analysis. The best fitting sinusoids to the pulse profiles obtained by folding the time series on the 264 s period yielded modulation depths of 24.7$\pm$4.6% and 16.9$\pm$4.2% for $\sim$ 0.1-1 keV and $\sim$ 1-2 keV energy bands, respectively. The quoted errors are at 1σ confidence level. The pulse profiles in the two energy bands are displayed in Figure 5.6. If we compare the 1-2 keV ROSAT modulation depth ($\sim$ 17%) with the 0.7-2 keV ASCA modulation depth ($\sim$ 12%), we see that they are consistent within the 1σ confidence level errors. Furthermore, the modulation depth measured in the 2-10 keV energy band of the ASCA data ($\sim$ 45%) is consistent with the quiescent modulation depth measured in the 3-10 keV energy band of the RXTE data ($\sim$ 40%; Szkody et al. 2002). The decrease in the pulse amplitude going from 0.1-1 keV to 1-2 keV is 7.8$\pm$6.2% ($\sim$ 1σ). Therefore, we find an evidence for a decreasing modulation depth up to $\sim$ 2 keV and then a very strong evidence for an increasing modulation up to 10 keV in the pulse profiles folded on the 264 s period of YY Dra.

Our results indicate that the photo-electric absorption is only relatively effective for the energies below $\sim$ 2 keV. The cross section of photo-electric absorption is related to the incoming photon energy with $\sigma \propto E^{-3.5}$. If we compare the absorption cross sections at 10 keV and 1 keV with the same absorbing column density, we find that the photons with energy of 1 keV are $\sim$ 3200 times more absorbed than the ones with 10 keV. Since the cross section of photo-electric absorption reduces by almost three orders of magnitude increasing from 1 keV to 10 keV, *for objects that show low absorbing column density like YY Dra* (see Table 5.1), the photons above $\sim$ 2 keV (almost) directly emerge as a narrow searchlight beam from the accretion column without being affected by photo-electric absorption, and only affected by electron scattering and occultation (the changing visibility of the post-shock region as the WD rotates). The combined affect above should, then, explain how the ASCA+ROSAT X-ray pulse profiles of YY Dra are produced. In addition, GK Per which is one of the fast rotating IPs show a decreasing pulse amplitude as the energy is increased (Norton & Watson 1989). This is not a surprising result, since the neutral hydrogen column density derived for GK Per is a factor of 10-100 higher than that of YY Dra and the absorption cross-section is directly proportional to the neutral hydrogen column density.

It is important to stress that both of the effects described above (electron scattering+occultation) are energy independent and does not explain the changing modulation depths. Then, one needs to introduce an extra effect either to increase the modulation in the X-rays above 2 keV or decrease the modulation

below 2 keV. If one assumes a stratified accretion column where the low temperature zone is at the base of the column, selectively, the lower energy photons will be intercepted more by the WD surface. Reflection from this surface (in one or multiple scatterings) will cause not the energy of the photons to change appreciably, but the direction θ could change considerably dispersing the incident beam. Thus, this should cause the modulation depths to diminish at the lower energies. It is quite difficult to constrain the accretion geometry of YY Dra with the data at hand since longer and better spectral resolution data are necessary for conclusive results. On the other hand, an alternative explanation to the reflection scenario is the changing visibility of the post-shock region in the accretion column together with the visibility of single or both of the accreting poles, however we stress that this is more difficult to model and less likely than the effect of reflection we suggested above. The reflection model is also consistent with the results from the RXTE data (Szkody et al. 2002) where the primary dominant pole is suggested to be occulted by the accretion disk during the outburst and only the secondary accretion pole is viewed. Thus, the modulation depths diminish to only about 7% which is, then, similar to the quiescent modulation depths below 2 keV calculated for YY Dra in this work. They must have detected the scattered and reflected radiation from the secondary accretion pole.

5.5.2 The Spectrum (0.1-10 keV)

Ezuka and Ishida (1999) have modeled 13 IPs by partial covering absorber model. They concluded that the X-ray spectrum of two of these 13 sources (EX

Hya and AE Aqr) required a two-temperature bremsstrahlung model , while for the rest, a single temperature model was adequate. Szkody et al. (2002) have modeled the RXTE spectrum of YY Dra in quiescence and in outburst by single temperature bremsstrahlung and Raymond-Smith models and noted that a multi-temperature model does not improve the fits considerably. We found that this is also true for the ASCA spectrum of YY Dra (see Table 5.2). We have also found that there is no need for a partial covering absorber model to interpret the data between 0.5-10 keV using the ASCA spectrum. This could be due to the low sensitivity of the SIS below 1 keV.

To investigate the spectrum at lower energies, we analyzed the ROSAT PSPC data of YY Dra taken on 2 October 1993, and modeled the ROSAT and ASCA spectrum simultaneously. The best fitted model parameters are tabulated in Table 5.3. The most important result from the simultaneous fitting of the data is the existence of a partial covering absorber of $20^{+15}_{-17}\%$ which is consistent with both of the data sets. This is a strong evidence in favor of our suggestion (scattering+reflection) to explain the energy dependence of the pulse profiles of YY Dra. The partial covering of the absorbing material implies a very complex absorbing medium with possible variable ionization states within the medium (i.e., warm absorber [Done et al. 1995]).

MCV spectra have also been elaborately modeled taking into account reflection from the WD surface and a temperature distribution within the post-shock region of the column (Beardmore et. al. 1995; Cropper et. al. 1998; Done &

Magdziarz 1998). These models require high signal-to-noise and spectral resolution data. Though, the ASCA or the ROSAT data of YY Dra does not have the necessary quality, we still applied the available models in XSPEC v11. in order to check the reliability of our suggestions. (e.g. ABSORI (Done et al. 1995; Zdziarski et al. 1990), HREFL, c6VMEKL and multi-temperature VMEKAL). Simultaneous fitting of ASCA and ROSAT spectra showed that a HREFL*VMEKAL model or a ABSORI*VMEKAL model yields satisfactory fits with a $\chi^2_\nu \sim 1.1$. However, the errors on the spectral parameters are high spanning large parameter spaces and determining a physical model becomes difficult. On the other hand, it shows that reflections/scatterings of the X-ray photons from the photo-sphere of the WD or from the pre-shock accretion column region plays a role in shaping of the spectrum as it does in shaping of the pulse profiles. Most likely, the accretion column is highly structured and the shock zone is stratified, X-rays emerging from the accretion column reflect from the WD surface and a warm partially ionized absorber exists in the pre-shock accretion column and/or the WD surface.

Fitting the VMEKAL model to the ASCA spectrum and to the ASCA+ROSAT spectrum simultaneously, we find an evidence for an iron K_α emission line at $\sim$ 7 keV with an abundance about half the Solar iron abundance (see Table 5.3). Moreover, small excess around 1 keV indicate the existence of Fe L-shell and the excess around 6.4 keV indicates the existence of Fe fluorescence emission lines in the spectrum. The non-detection of the iron lines in YY Dra suggests either the abundance of iron is low as derived from the spectrum (see Table 5.1, 5.2

and 5.3) or another mechanism is present that smears the emission lines and making it difficult to resolve them from the continuum. We suggest that given the conditions described above the resonance absorption of the line photons as suggested before for other MCVs (Hellier, Mukai, Osborne 1998; Tesseling et al. 1999) could be responsible for the disappearance of the iron lines in YY Dra, as well. The identification of the iron lines could be possible via an observation with the CHANDRA, HETG (High Energy Transmission Grating).

Table 5.1: Single-temperature bremsstrahlung and VMEKAL model parameters

Model	Bremsstrahlung	VMEKAL
$N_H(10^{22}cm^{-2})$	$0.042^{+0.040}_{-0.036}$	0.047 ± 0.036
kT_1 (keV)	$7.9^{+4.7}_{-2.3}$	$7.2^{+3.6}_{-1.8}$
Fe_1 (Solar)	-	<1
$Norm_1$ (cm^{-5})	$3.7^{+0.7}_{-0.8} \times 10^{-3}$	$1.0\pm0.1\times10^{-2}$
χ^2_ν	$\sim$0.9	$\sim$0.9

Table 5.2: Two-temperature bremsstrahlung and VMEKAL model parameters

Model	Bremsstrahlung	VMEKAL
$N_H(10^{22}cm^{-2})$	$0.28^{+0.04}_{-0.03}$	$0.08^{+0.10}_{-0.06}$
kT_1 (keV)	$0.37^{+30}_{-0.22}$	$0.97^{+0.36}_{0.59}$
Fe_1 (Solar)	-	$0.53^{+0.50}_{-0.48}$
$Norm_1$ (cm^{-5})	$2.5^{+10.5}_{-1.0} \times 10^{-2}$	$9.7^{+27.0}_{-7.3} \times 10^{-4}$
kT_2 (keV)	$13.59^{+21.41}_{-7.59}$	$11.56^{16.44}_{-6.06}$
Fe_2 (Solar)	-	<1.5
$Norm_2$ (cm^{-5})	$3.5^{+0.5}_{-0.4} \times 10^{-3}$	$9.4^{+1.2}_{-1.3} \times 10^{-3}$
χ^2_ν	$\sim$0.8	$\sim$0.7

Table 5.3: Simultaneous fitting of ASCA and ROSAT Data

Model	Pcfabs*VMEKAL
N_H (cm^{-2})	$0.15^{+0.55}_{-0.15}$
CvrFrac	$0.20^{+0.14}_{-0.18}$
kT (keV)	$7.4^{+2.8}_{-1.5}$
Fe (Solar)	$0.49^{+0.41}_{-0.37}$
Norm (ROSAT) (cm^{-5})	$3.88^{+0.47}_{-0.42} \times 10^{-3}$
Norm (ASCA) (cm^{-5})	$3.67^{+0.27}_{-0.24} \times 10^{-3}$
χ^2_ν	$\sim$1.1

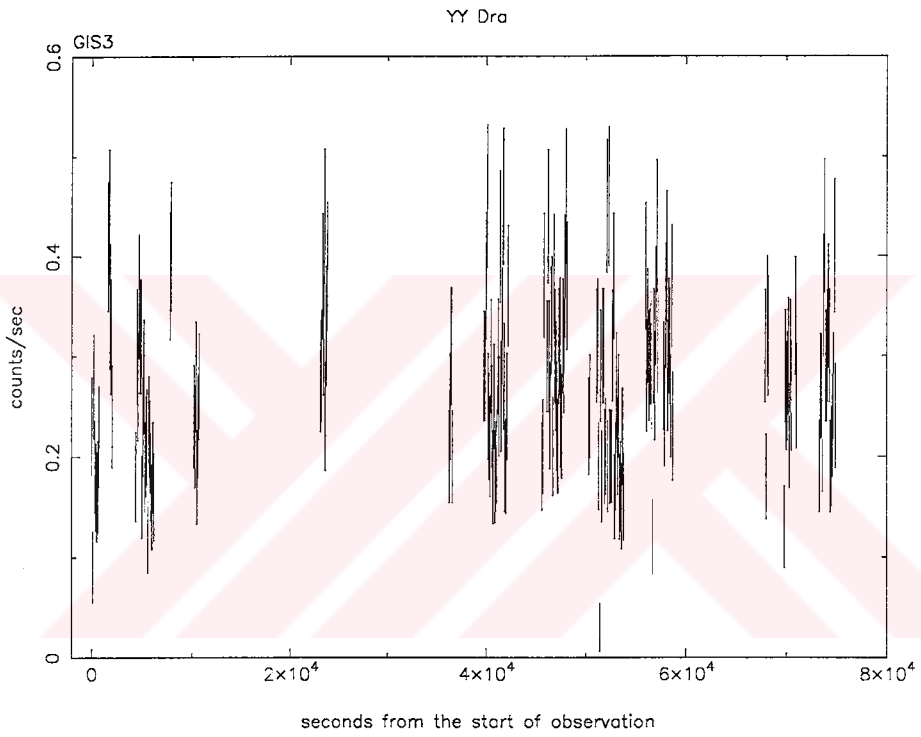


Figure 5.1: X-ray light curve of YY Dra in 100 sec bins

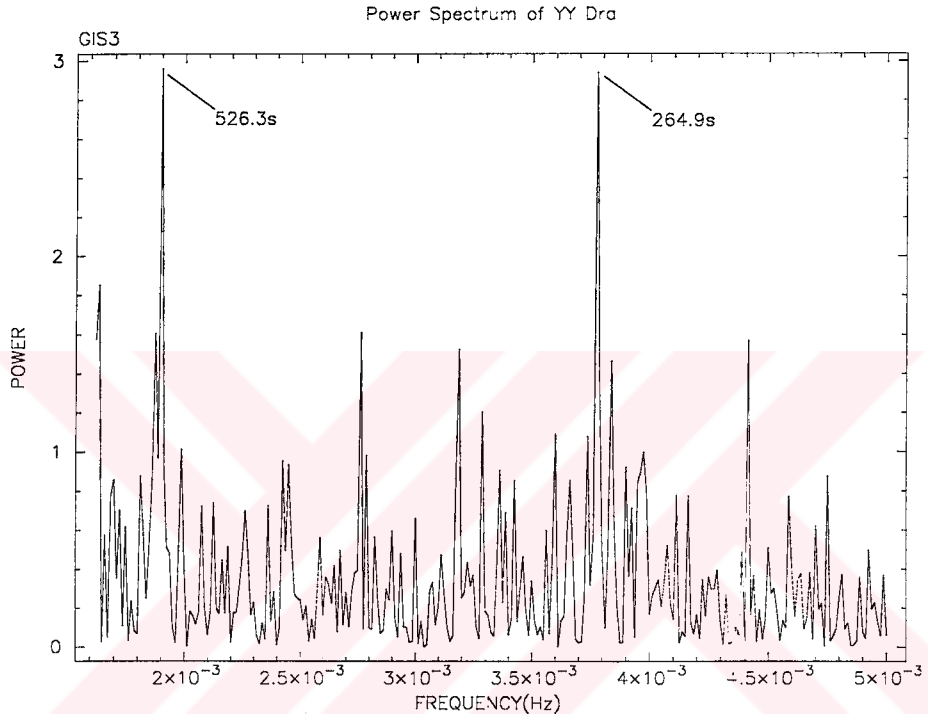


Figure 5.2: The Power Spectrum of YY Dra obtained using data from the GIS3 detector on board ASCA showing signals at 526.3 sec and 264.9 sec. In constructing the power spectrum, 10 sec. binned light curve is used.

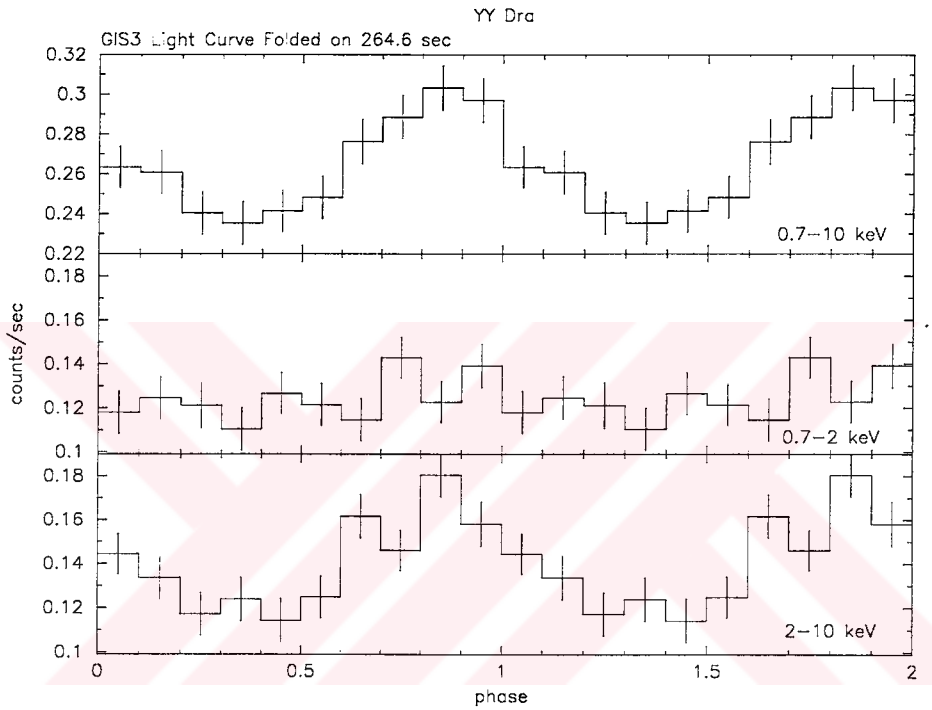


Figure 5.3: The energy dependent folded pulse profiles of YY Dra obtained from the GIS3 data folded on the 264.6 s period. The upper panel shows the pulse profile folded on the 264.6 sec period in the total energy range (0.7-10 keV). The middle panel shows the profiles in 0.7-2 keV energy band and the bottom panel shows the profiles in 2-10 keV energy band.

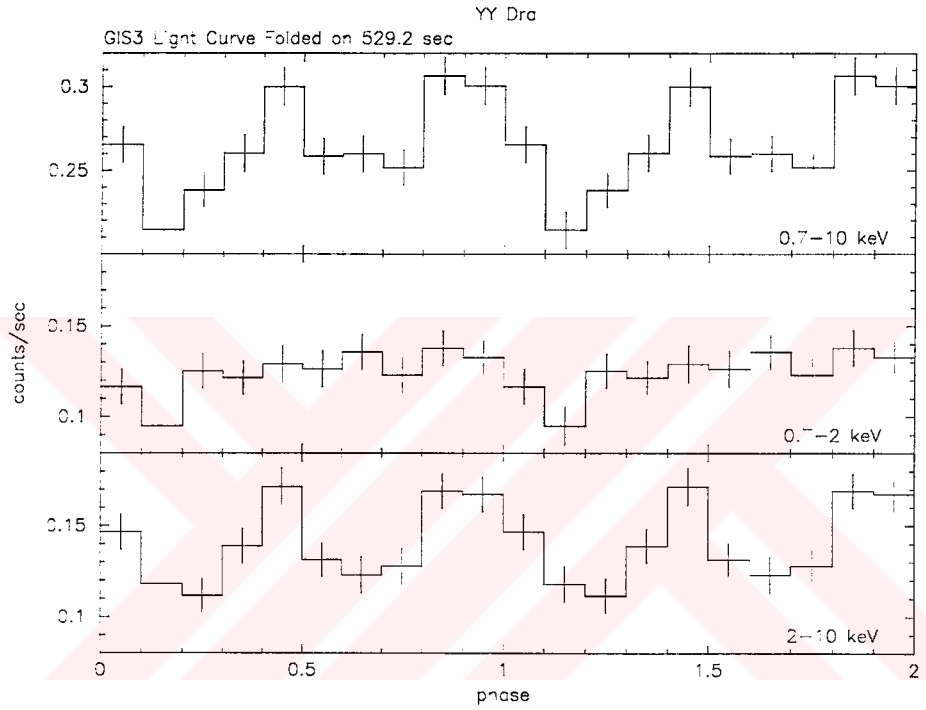


Figure 5.4: The energy dependent folded pulse profiles of YY Dra obtained from the GIS3 data folded on the 529.2 s period. The upper panel shows the pulse profile folded on the 529.2 sec period in the total energy range (0.7-10 keV). The middle panel shows the profiles in 0.7-2 keV energy band and the bottom panel shows the profiles in 2-10 keV energy band.

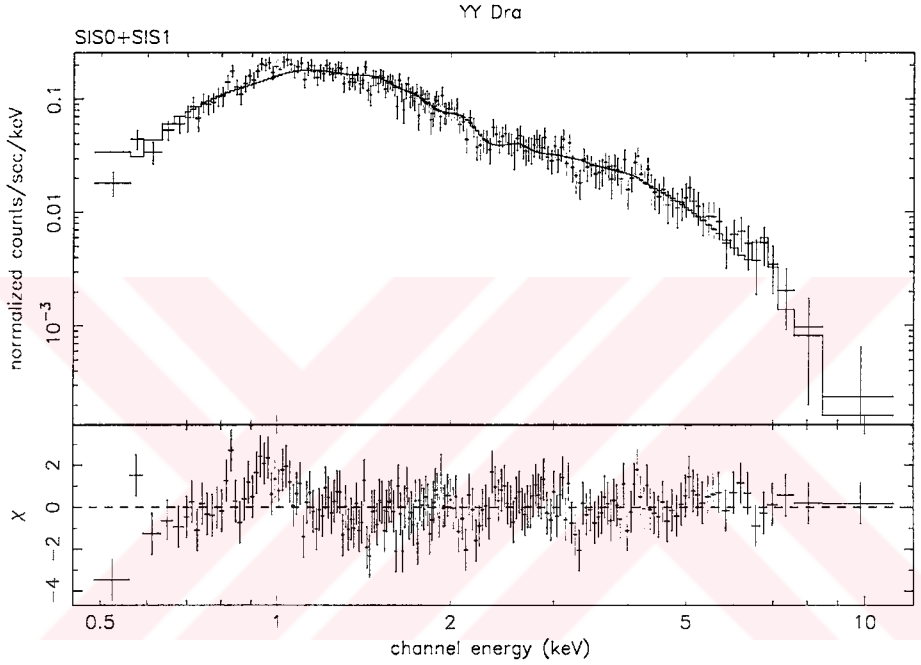


Figure 5.5: The X-ray data of YY Dra fit with a single-temperature VMEKAL model including neutral hydrogen absorption. Crosses represent the data and the smooth curve represent the model fitted to the spectrum of YY Dra. The lower panel shows the residuals between the data and the model in standard deviations.

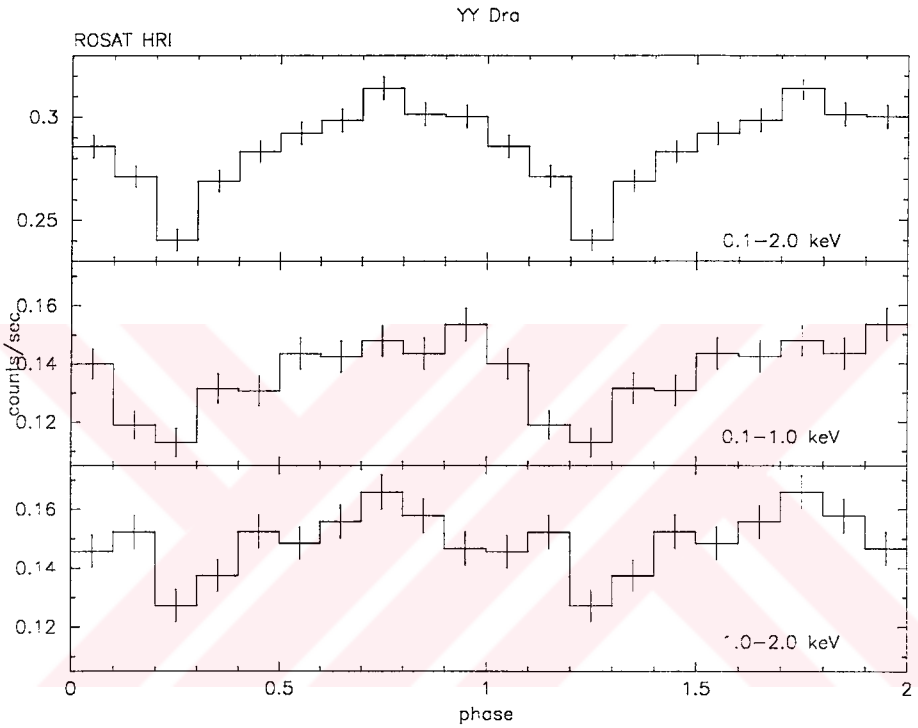


Figure 5.6: The energy dependent folded pulse profiles of YY Dra obtained from ROSAT HRI data. The upper panel shows the pulse profile folded on the 264.6 sec period in the total energy range (0.1-2.0 keV). The middle panel shows the profiles in 0.1-1.0 keV energy band and the bottom panel shows the profiles in 1.0-2.0 keV energy band.

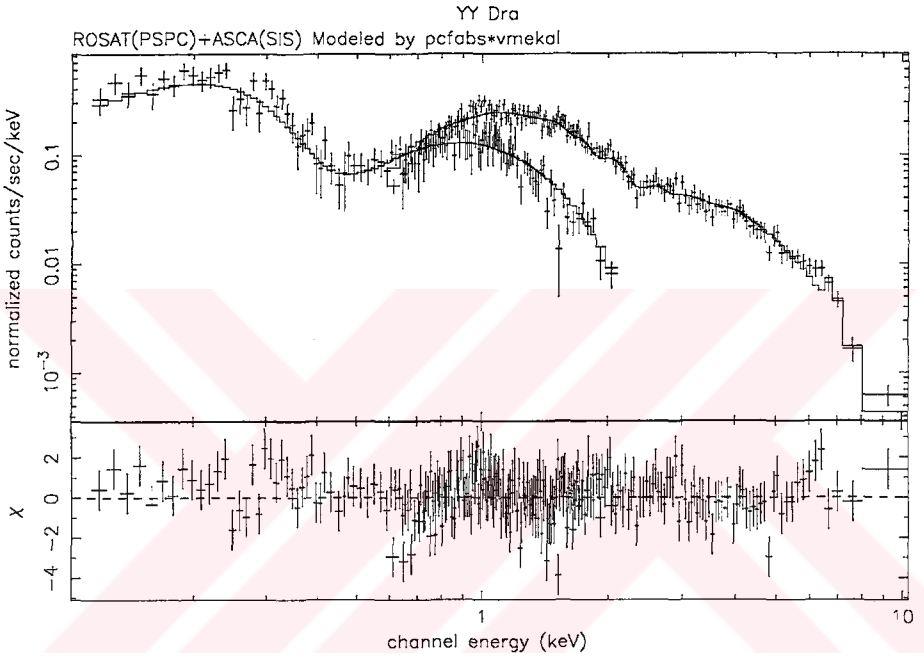


Figure 5.7: The combined spectrum of ROSAT (HRI) and ASCA (SIS) data of YY Dra fitted with a single-temperature VMEKAL emission model including a partial covering absorber. Crosses represent the data and the smooth curve represent the model fitted to the spectrum of YY Dra. The lower panel shows the residuals between the data and the model in standard deviations.

CHAPTER 6

DISCUSSION AND CONCLUSIONS

In this thesis, an up-to-date review of intermediate polar type cataclysmic variables are made emphasizing timing characteristics. Fundamental timing analysis methods are introduced. Timing analysis on the intermediate polar AE Aquarii is performed using three sets of *ROSAT* archival data. As a result of the analysis, the period of AE Aquarii is confirmed and an orbital sideband is found, the first harmonic of the spin period proposed by other authors could not be detected. An indication of a changing period or changing accretion geometry is found from the pulse profiles.

We have presented a joint analysis of the ASCA and ROSAT data of the IP YY Dra in the last section. Our results show that the accretion column environment of YY Dra is very complex and structured. We suggest that most likely, the accretion column is stratified and the lower energy photons, selectively produced at the base of the accretion column (i.e. due to the cooling in the column) suffer reflections/scatterings from the WD surface causing diminishing modulation depths in the X-ray light curve at lower energies. However, we do not rule out

occultation of the post-shock region via a complex accretion geometry to produce pulse profiles at hand. Our individual results on YY Dra include:

1) Rotation period of the WD in YY Dra is confirmed to be 526.3±3.5 s, which covers the previously published period for this source within the error range. We also detect a co-dominant peak at the first harmonic of the spin period suggesting accretion on both poles of YY Dra.

2) Modulation depth of the X-ray pulses of YY Dra has a complex energy dependence, which decreases below 2 keV (1σ) and increases above 2 keV (3σ) as energy is increased.

3) We find that ASCA spectrum of YY Dra can be reasonably fit using a single temperature VMEKAL*photoelectric absorption model with kT=$7.2^{+3.6}_{-1.8}$ keV, and N_H=$4.7^{+3.6}_{3.6} \times 10^{20}$ cm^{-2}. Thus, YY Dra is one of the coolest IPs after AE Aqr and EX Hya and it also has less neutral column density obscuring the X-ray emitting region, compared to other IPs. On the other hand, simultaneous fitting of ASCA and ROSAT data requires modelling with partial covering 20^{+14}_{-18}% of the absorbing medium with N_H=$1.5^{+5.5}_{-1.5} \times 10^{21}$ cm^{-2} that is still low. This shows that the absorbing medium in YY Dra is very complex with possible variable ionization states of material inside.

4) Simultaneous fitting of ASCA and ROSAT showed that HREFL, ABSORI, c6VMEKAL and multi-temperature VMEKAL models are consistent with the data. This, then, would be a strong indication of stratification in the accretion column with the high temperature material at the top and low temperature material at the base of the column resulting in detections of different temperatures

in the X-ray spectrum. On the other hand, we caution that the quality of the data at hand is not suitable for discrimination of the best physical model for the source. The analysis on YY Dra shows that, it has quite a unique environment detected in X-rays in comparison with other IPs. This makes the source an excellent laboratory among MCVs to study the effects of reflection, scattering, and line formation in structured and stratified accretion columns. Detailed observations of YY Dra by CHANDRA grating facilities would be valuable in determining the spectral parameters using more realistic and complicated models providing insight into the pulse production mechanisms and the observed spectrum from YY Dra.

REFERENCES

[1] Balachandran S., Robinson E.L., Kepler S.O, 1983, PASP, 95, 1062

[2] Barrett P.E., O'Donoghue D., and Warner B.. 1988, MNRAS, 233, 759

[3] Beardmore A.P., Done C., Osborne J.P., and Ishida M., 1995, MNRAS, 272, 749

[4] Berriman G., Bailey J., Axon D.J., Hough J.H., 1986, MNRAS, 223, 449
Bianchini A., Sabbadin F., Hamzaoglu E., 1981, A&A, 99, 392

[5] Beuermann K., Thomas H.-C., 1993, Adv. Space. Res., 13(12), 115

[6] Brigham E.O., 1974, The Fast Fourier Transform (Englewood Cliffs, NJ: Prentice Hall)

[7] Burke B.E., Mountain R.W., Harrison D.C.. Bautz M.W., Doty J.P., Ricker G.R., and Daniels P.J., 1991, IEEE Trans. ED-38, 1069

[8] Cherepashchuk A.M., Katysheva N.A., Khuzina T.S., Shugarov S.Y., 1996, 'Highly Evolved Close Binary Stars: Finding Charts', Gordon and Breach

[9] Chiappetti L., Belloni T., Bonnet-Bidaut, del Gratta J.M., de Martino D., Maraschi L., Mouchet M., Mukai K., Osborne J.P., Corbet R.H.D., Tanzi E.G., Treves A., 1989, ApJ, 342, 493

[10] Chincarini G., Walker M.F., 1981, A&A, 104. 24

[11] Crampton D., Fisher W.A., Cowley A.P., 1986, ApJ, 300, 788

[12] Cropper M., Ramsay G., and Wu K., 1998, MNRAS, 293, 222

[13] de Jager, O.C., 1991, ApJ, 378, 286

[14] de Jager O.C., Meintjes P.J., O'Donoghue D.. Robinson E.L., 1994, MNRAS, 207, 577

[15] Done C., Osborne J.P., and Beardmore A.P.. 1995, MNRAS, 276, 483

[16] Done C. and Magdiziarz P., 1998 MNRAS, 298, 737

[17] Downes R.A., Shara M.M. 1993, PASP, 105, 127

[18] Eracleous M., Halpern J., and Patterson J., 1991, ApJ, 382, 290

[19] Eracleous M., 1999, Annapolis Workshop on Magnetic Cataclysmic Variables, ASP Conference Series, Volume 157, edited by Coel Hellier and Koji Mukai, 1999, p. 343

[20] Ezuka H., and Ishida M., 1999, ApJSS, 120, 277

[21] Feldth A.N. and Chincarini G., 1980, PASP, 92, 258

[22] Frank J., King A.R., and Lasota J.P., 1988, A&A, 193, 113

[23] Friend F., Martin J.S., Smith R.C., and Jones D.H.P., 1988, MNRAS, 233, 451

[24] Ghosh P., Lamb F.K. 1979a, ApJ, 232, 259

[25] Ghosh P., Lamb F.K. 1979b, ApJ, 234, 296

[26] Ghosh P., Lamb F.K. 1991, in Neutron Stars: Theory and Observation, Kluwer Academic Publishers, eds. J. Ventura, D. Pines, 1991, p.363-444

[27] Haberl F., Thorstensen J.R., Motch C., Schwarzenberg-Czerny A., Pakull M., Shabrook A., and Pietsch W., 1994, A&A, 291, 171

[28] Haswell C.A., Patterson J., Thorstensen J.R., Hellier C., Skillman D.R., 1997, ApJ, 476, 847

[29] Heise J., Mewe R., Kruzewski A., Chebowski T., 1987, A&A, 183, 73

[30] Hellier C., 1991, MNRAS, 251, 693

[31] Hellier C., 1992, MNRAS, 258, 578

[32] Hellier C., Cropper M.S., and Mason K.O., 1991, MNRAS, 248, 233

[33] Hellier C., 1999, in 'Annapolis Workshop on Magnetic Cataclysmic Variables', eds., C. Hellier, K. Mukai,ASP Conf. Ser.V.157, p.1-13

[34] Hellier C., Mukai K., and Osborne J.P., 1998 MNRAS, 297, 526

[35] Horne J.H., and Baliunas S.L., 1986, ApJ., 302, 757

[36] Hutchings J.B., 1987, PASP, 99, 57

[37] Ishida M., Mukai K., Osborne J.P., 1994, PASJ, 46L

[38] Jablonski F., 1981, IBVS, 1911,1

[39] Jensen K.A., 1985, IAUC, 4102,3

[40] Kaastra J.S., 1992, An X-ray Spectral Code for Optically Thin Plasmas (Internal SRON-Leiden Report, updated version 2.0)

[41] Kellogg A., Baldwin C. and Koch J., 1975, ApJ, 199, 299

[42] King A.R., and Shaviv G., 1984, MNRAS, 211, 883

[43] King A.R., and Lasota J.P., 1991, ApJ, 378, 674

[44] Klis M., 1989, in Timing Neutron Stars, eds. H. Ogelman and E.P.J. van den Heuvel, Kluwer Academic Publishers.

[45] Kubiak M., 1983, Msngr, 34,33

[46] Kubiak M., 1984,AcA,34,397

[47] Kuijpers G., and Pringle J.E., 1982, A&A, 114, L4

[48] Kruszewski A., Semeniuk I., 1998 Acta Astronomica, 48, 757

[49] Kylafis N.D., and Lamb D.Q., 1982, ApJS, 48, 239

[50] Lamb D.Q. 1988, in Polarized Radiation of Circumstellar Origin, ed. G.V. Coyne et al. (Vatican, Vatican Observatory), p.153

[51] Lomb N.R., 1976, Astr. Spa. Sci., 39, 447

[52] Longair M., 1992, High Energy Astrophysics, Cambridge University Press, p.89

[53] Makishima K., et al., 1996, PASJ, 48, 171

[54] Martell P.J., Horne K., Price C.M., Gomer R.H., 1995, ApJ, 448, 380

[55] Mason M., Szkody P., and Garnavich P., 1991, ApJ, 370, 370

[56] Mason K.O., et al., 1992, MNRAS, 258, 749

[57] Mason K.O., 1995, ASP conf. ser. v.85, 225

[58] Mason K.O., 1997, MNRAS, 285, 493

[59] Mateo M., Szkody P., Garnavich P., 1991, ApJ, 370, 370

[60] Mewe R., Gronenschild E.H.B.M., and van den Oord G.H.J., 1985, A&AS, 62, 197

[61] Meintjes P.J., Raubenheimer B.C., de Jager O.C., et al., 1992, ApJ., 401, 325

[62] Morrison R. and McCammon D., 1983, ApJ, 270, 119

[63] Mouchet M., Bonnet-Bidaud J.M., Buckley D.A.H., Tuohy I.R., 1991, A&A, 250,90

[64] Mumford G.S., 1967, ApJss, 15,1

[65] Murray J.R., Armitage P.J., Ferrario L. et al.. 1999, MNRAS, 302, 189

[66] Norton A.J., and Watson M.G., 1989, MNRAS, 237, 853

[67] Norton A.J., Watson M.G., King A.R., 1988, MNRAS, 231, 783

[68] Norton A.J., and Watson M.G., 1990, in Accretion-Powered Compact Binaries, ed. C. Mauche (Cambridge, Cambridge University), p. 209

[69] Norton A.J., Watson M.G., Hing A.R., Lehto H.J., and McHardy, I.M., 1992a, MNRAS, 254, 705

[70] Norton A.J., McHardy I.M., Lehto H.J., and Watson M.G., 1992b, MNRAS, 258, 697

[71] Norton A.J., Beardmore A.P., Allan A., and Hellier C., 1999, A&A, 347, 203

[72] Norton A.J., Beardmore A.P., Retter A., Buckley D.A.H., 2000, MNRAS, 312, 362

[73] Ohashi T. et al., 1996, PASJ, 48, 157

[74] Osborne J.P., Rosen R., Mason K.O., Beuermann K., 1985, SSRv, 40, 143

[75] Osborne J., Mukai K., 1989, MNRAS, 238,1233

[76] Pakull M.W. and Beuermann K., 1987, ApJSS, 131, 641

[77] Patterson J., 1979, ApJ, 234, 978

[78] Patterson J., 1979, ApJL, 233, 13

[79] Patterson J., Branch D., Chincarini G., Robinson E.L., 1980, ApJL, 240, 133

[80] Patterson J., Schwartz D.A., Pye J.P., Blair W.P., Williams G.A., Caillault J.P., 1992, ApJ, 392, 233

[81] Patterson J., Moulden M., 1993, PASP, 105, 779

[82] Patterson J., Paula S., 1993, PASP, 105,1116

[83] Patterson J., 1994, PASP, 106, 209

[84] Patterson J., 1988 IBVS, 3264,1

[85] Patterson J., Beurmann K., Africano J., 1988, BAAS, 20, 1099

[86] Patterson J., Kemp J.,Richman H.R., Skillman D.R., Vanmunster T., Jensen L., Buckley D.A.H., O'Donoghue D., Kramer R., 1998, PASP, 110, 415

[87] Potter S.B., Cropper, M., Mason K.O., Hough J.H., Bailey J.A., 1997, MNRAS, 285, 82

[88] Press W.H., and Rybicki G.B., 1989, ApJ, 338, 277

[89] Press W.H., Teukolsky S.A., Vetterling W., and Flannery B.P., 1996, Numerical Recipes in Fortran 77, Cambridge University Press

[90] Raymond J.C. and Smith B.W., 1977, ApJSupp., 35, 419

[91] Reilman R.F., and Manson S.T., 1986, ApJS, 62, 939

[92] Reinsch K., Beuermann K., Hanusch H., Thomas H.C., 1995, in Cape Workshop on Magnetic Cataclysmic Variables, PASP Conf. Ser. vol. 85, eds. D.A.H. Buckley and B. Warner, p.115

[93] Richman H.R., 1996, ApJ, 462, 404

[94] Robinson E.L., Clemens J., Christopher H., Butler P., 1988, ApJL, 331, 29

[95] Robinson E.L., Shafter A.W., Balachandran S., 1991, ApJ, 374, 298

[96] Rosen S.R., 1992, MNRAS, 254, 493

[97] Rosen S.R., Mason K.O., and Cordova F.A., 1988, MNRAS, 231, 549

[98] Scargle J.D., 1982, ApJ, 263, 835

[99] Schlegel E.M., 1999, ASP Conf ser vol.157,p.60

[100] Seetha S., Sharma D.P., Padmini V.N., Marar T.M.K., Kasturirangan K., 1987, Ap&SS, 130, 193

[101] Shafter A.W., Szkody P., and Thorstensen J., 1986, ApJ, 308, 765

[102] Shafter A.W., Macry J.P., 1987, MNRAS, 228, 193

[103] Shakhovskoy N.M., Andronov I.L., Kolesnikov S.V., 2001, AGM, 18, P16

[104] Silber A.D., Anderson S.F., Margon B., Downes R.A., 1996, ApJ, 462, 428

[105] Singh J., Agrawal P.C., Apparao M.V.K., Manchanda R.K., Vivekananda R.P., Sarma M.B.K., 1991, PASAu, 9, 279

[106] Smith R.C., 1995, Observational Astrophyics, Cambridge University Press

[107] Stavroyiannopoulos D., Rosen S.R., Watson M.G., Mason, K.O., Howell, S.B., 1997, MNRAS, 288

[108] Szkody P., Nishikida K., Erb D., Mukai K., Hellier C., Uemura M., Kato T., and Cook L., 2002, AJ, in press.

[109] Thompson A.M., Brown J.C., and Kuijpers J., 1986, A&A, 159, 202

[110] Thorstensen J.R., 1997, PASP, 109, 1241

[111] Thorstensen J.R. and Taylor C.J., 2000. MNRAS, 312, 629

[112] Uslenghi M., Bergamin P., Catalano S., Tommasi L., Treves A., A&A 2000, 359, 639

[113] van Amerongen S., Augusteijn T., van Paradijs T., 1987, MNRAS, 228, 377

[114] van Teeseling A., Fischer A., and Beuermann K., in 'Annapolis Workshop on Magnetic Cataclysmic Variables', eds. C. Hellier and K. Mukai, p.309-316

[115] Vogt N., Krzeminski W., Sterken C., 1980, A&A, 85, 106

[116] Warner B., Cropper M., 1984, MNRAS, 206, 261

[117] Warner B., and Wickramasinghe D.T., 1991, MNRAS, 248, 370

[118] Watson M.G., Smith A., 1983, IAUC, 3856,4

[119] Watson M.G., King A.R., Osborne J., 1985, MNRAS, 212, 917

[120] Warner B., 1995, Cataclysmic Variable Stars, Cambridge University Press, Cambridge

[121] Wenzel W., 1983, IBVS, 2262

[122] Wickramasinghe D.T., Wu K., and Ferrario L., 1991, MNRAS, 249, 460

[123] Wickramasinghe D.T., and Ferrario L., in Annapolis Workshop on Magnetic Cataclysmic Variables, ASP Conference Series, Volume 157, edited by Coel Hellier and Koji Mukai, 1999, p. 15

[124] Williams G.A., King A.R., Watson M.G., 1984, MNRAS, 207, 17

[125] Yamashita A., et al., 1997, IEEE Trans. Nucl. Sci. 44, 847

[126] Zdziarski et al. 1995, ApJ, 363, L1

[127] Zhang E., Robinson E.L., Stiening R.F., Horne K., 1995, ApJ, 454, 447

T.C. YÜKSEKÖĞRETİM KURULU
DOKÜMANTASYON MERKEZİ

[128] Zharikov S.V., Tovmassian G.H., Echevarria J., Cardenas A.A, A&A 2001, 366, 834

[129] Zimmermann H.U., et al., 1994, EXSAS User's Guide, ROSAT Scientific Data Center.

[130] Zombeck M.V., David L.P., Harnden F.R., Kearns K., 1995, Proc. SPIE 2518, 304

T.C. YÜKSEKÖĞRETİM KURULU
DOKÜMANTASYON MERKEZİ